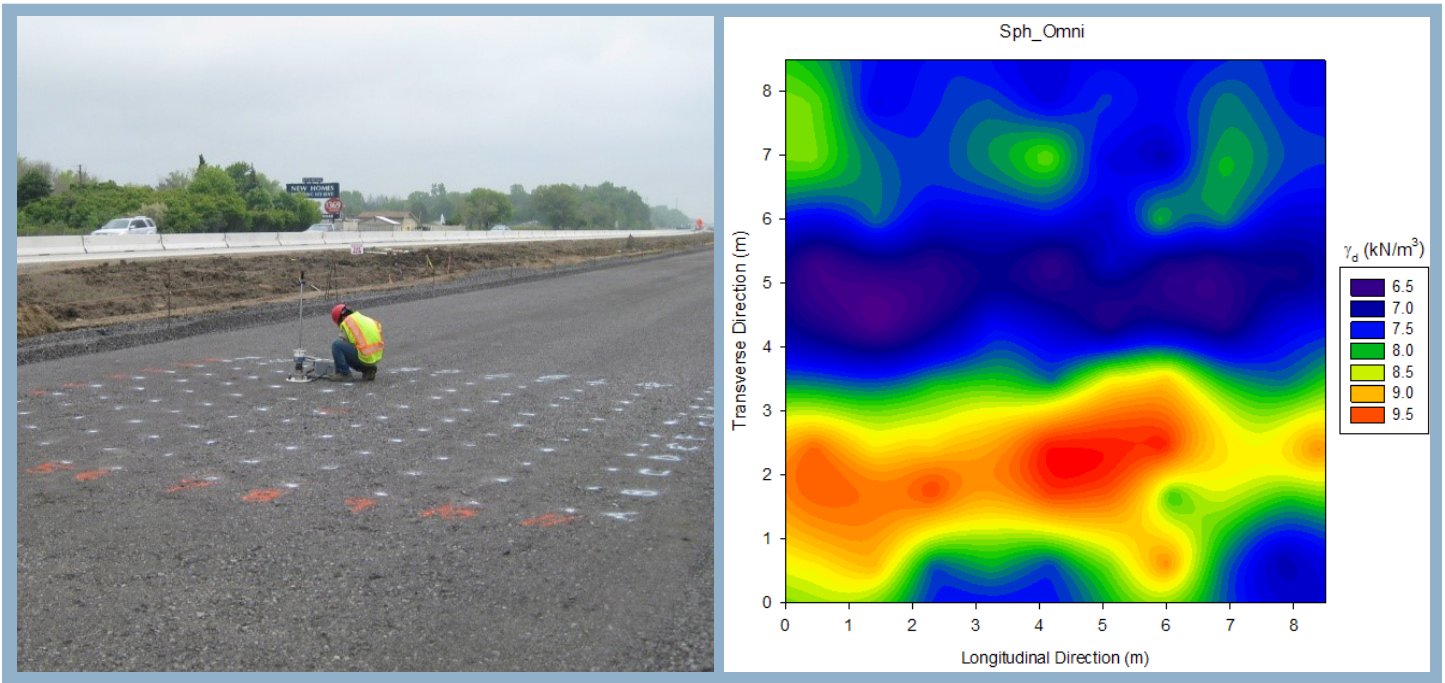# Improving the Foundation Layers for Concrete Pavements

## TECHNICAL REPORT:
## Field Assessment of Variability in Pavement Foundation Properties



**April 2018**

National Concrete Pavement Technology Center

CP Tech Center

CENTER FOR CEER EARTHWORKS ENGINEERING RESEARCH

IOWA STATE UNIVERSITY
Institute for Transportation

## About the National CP Tech Center

The mission of the National Concrete Pavement Technology (CP Tech) Center is to unite key transportation stakeholders around the central goal of advancing concrete pavement technology through research, tech transfer, and technology implementation.

## About CEER

The mission of the Center for Earthworks Engineering Research (CEER) at Iowa State University is to be the nation's premier institution for developing fundamental knowledge of earth mechanics, and creating innovative technologies, sensors, and systems to enable rapid, high quality, environmentally friendly, and economical construction of roadways, aviation runways, railroad embankments, dams, structural foundations, fortifications constructed from earth materials, and related geotechnical applications.

## Disclaimer Notice

## Iowa State University Non-Discrimination Statement

## Iowa Department of Transportation Statements

**Technical Report Documentation Page**

| 1. Report No.<br>DTFH 61-06-H-00011 Work Plan 18 | 2. Government Accession No. | 3. Recipient's Catalog No. | |
|---|---|---|---|
| 4. Title and Subtitle<br>Improving the Foundation Layers for Concrete Pavements:<br>Field Assessment of Variability in Pavement Foundation Properties | | 5. Report Date<br>April 2018 | |
| | | 6. Performing Organization Code | |
| 7. Author(s)<br>Jia Li, David J. White, and Pavana K. R. Vennapusa | | 8. Performing Organization Report No.<br>InTrans Project 09-352 | |
| 9. Performing Organization Name and Address<br>National Concrete Pavement Technology Center and<br>Center for Earthworks Engineering Research (CEER)<br>Iowa State University<br>2711 South Loop Drive, Suite 4600<br>Ames, IA 50010-8664 | | 10. Work Unit No. (TRAIS) | |
| | | 11. Contract or Grant No. | |
| 12. Sponsoring Organization Name and Address<br>Federal Highway Administration<br>U.S. Department of Transportation<br>1200 New Jersey Avenue SE<br>Washington, DC 20590 | | 13. Type of Report and Period Covered<br>Technical Report | |
| | | 14. Sponsoring Agency Code<br>TPF-5(183) | |
| 15. Supplementary Notes<br>Visit www.cptechcenter.org or www.ceer.iastate.edu for color PDF files of this and other research reports. | | | |

**16. Abstract**

This technical project report is one of the field project technical reports developed as part of the TPF-5(183) and FHWA DTFH 61-06-H-00011:WO18 studies.

Non-uniform support conditions under pavements can have detrimental effects on the service life of pavements. Generally, pavement design considers the foundation as a layered medium with spatially uniform material properties and support conditions. But, soil engineering parameters generally show significant spatial variation. In this report, field testing was conducted at several pavement foundation construction sites in a dense grid pattern with relatively close spacing (i.e., < 1 m) over a small area (< 10 m x 10 m) and in a sparse sampling pattern (> 5 m apart) over a large area (> 100 m) to characterize spatial variability. Results from selected field studies were analyzed for a more in-depth analysis of spatial variability and assessment of anisotropy. The measurement parameter values assessed include elastic modulus determined from the light weight deflectometer (LWD) test, penetration index of subbase and subgrade layers using dynamic cone penetrometer (DCP) test, and dry unit weight and moisture content determined from the nuclear gauge (NG) test method. Spatial variability analysis on dense gridded test sections showed that different anisotropic major directions could be expected in different test areas. Results showed that the correlation lengths are about 2 m to 3 m in the minor direction, and the correlation length in the major direction is about 3 to 4 times large than the minor direction, which indicates more uniformity in the major direction than in the minor direction. Comparisons of directional semivariogram models from dense and sparse datasets from the same project are also provided in this report. Results showed range values between 2 m and 11 m for dense gridded datasets taken over a relatively small area versus range values between 15 m to 45 m for sparse datasets taken over large areas. Longer ranges represent more spatially continuous data with longer correlation lengths than shorter ranges. The longer ranges in the sparse dataset compared to shorter ranges calculated using the dense grid dataset suggests that there is a nested structure in the data with both short and long range spatial continuity of the measured properties. In summary, the data and analysis demonstrate that spatial variability in pavement foundation layers can be quantified using semivariogram modeling, but is anisotropic and depends on test spacing.

| 17. Key Words<br>concrete pavement—pavement foundation—quality assurance—quality control—geostatistics—spatial analysis—subbase—subgrade | | 18. Distribution Statement<br>No restrictions. | |
|---|---|---|---|
| 19. Security Classification (of this report)<br>Unclassified. | 20. Security Classification (of this page)<br>Unclassified. | 21. No. of Pages<br>68 | 22. Price<br>NA |

**Form DOT F 1700.7 (8-72)**          **Reproduction of completed page authorized**

# IMPROVING THE FOUNDATION LAYERS FOR CONCRETE PAVEMENTS: FIELD ASSESSMENT OF VARIABILITY IN PAVEMENT FOUNDATION PROPERTIES

**Technical Report**
April 2018

**Research Team Members**
Tom Cackler, David J. White, Jeffery R. Roesler, Barry Christopher, Andrew Dawson,
Heath Gieselman, Pavana Vennapusa

**Report Authors**
Jia Li, Ph.D.
David J. White, Ph.D., P.E.
Pavana K. R. Vennapusa, Ph.D., P.E.

**National Concrete Pavement Technology Center and
Center for Earthworks Engineering Research (CEER)**
Iowa State University
2711 South Loop Drive, Suite 4700
Ames, IA 50010-8664
Phone: 515-294-5798
www.cptechcenter.org and www.ceer.iastate.edu

# TABLE OF CONTENTS

# LIST OF FIGURES

# LIST OF TABLES

# ACKNOWLEDGMENTS

# EXECUTIVE SUMMARY

Quality foundation layers (the natural subgrade, subbase, and embankment) are essential to achieving excellent pavement performance. Unfortunately, many pavements in the United States still fail due to inadequate foundation layers. To address this problem, a research project, Improving the Foundation Layers for Pavements (FHWA DTFH 61-06-H-00011 WO #18; FHWA TPF-5(183)), was undertaken by Iowa State University (ISU) to identify, and provide guidance for implementing, best practices regarding foundation layer construction methods, material selection, in situ testing and evaluation, and performance-related designs and specifications. As part of the project, field studies were conducted on several in-service concrete pavements across the country that represented either premature failures or successful long-term pavements. A key aspect of each field study was to tie performance of the foundation layers to key engineering properties and pavement performance. In-situ foundation layer performance data, as well as original construction data and maintenance/rehabilitation history data, were collected and geospatially and statistically analyzed to determine the effects of site-specific foundation layer construction methods, site evaluation, materials selection, design, treatments, and maintenance procedures on the performance of the foundation layers and of the related pavements. A technical report was prepared for each field study.

In this report, results from selected field studies were analyzed for a more in-depth analysis of spatial variability and assess anisotropy in the different measurements. The following selected measurement parameters were assessed: a) elastic modulus determined from the light weight deflectometer (LWD) test ($E_{LWD-Z3}$), b) dynamic cone penetration index (DCPI) of subbase layer and subgrade layers ($DCPI_{subbase}$, and $DCPI_{subgrade}$) using dynamic cone penetrometer (DCP) test, and c) dry unit weight ($\gamma_d$) and moisture content ($w$) determined from the nuclear gauge (NG) test method. Results were analyzed on test sections where two different sampling methods were followed: a) dense grid sampling with spacing less than 1 m over a relatively short area (< 10 m x 10 m area) and b) sparse sampling with test locations separated by 4 to 5 m and over a relative large area (100 to 500 m).

Detailed geostatistical analysis procedures are presented in this report to provide a guide to study spatial variability of pavement foundation properties with consideration of choosing the best fitted semivariogram model and characterization of anisotropic behavior. Anisotropy in pavement foundation properties is assessed using directional semivarigrams in comparison with omnidirectional experimental semivariograms, rose diagrams (identifying semivarigoram range values in different directions), semivariogram maps, and semivariogram contour maps.

Spatial variability analysis on dense gridded test sections showed that different anisotropic major directions could be expected in different test areas. One of the dense gridded test section showed that the transverse direction is more uniform than the longitudinal direction and another dense gridded test section showed the opposite. Results showed that the correlation lengths are about 2 m to 3 m in the minor direction and the correlation length in the major direction is about 3 to 4 times as the minor direction, which indicates more uniformity in the major direction than in the minor direction. The identified behaviors represented a relatively small sampling area that equaled the width of the foundation layer and about the same length in the longitudinal direction,

so they cannot be generalized for a more larger area in a given project. More data in the longitudinal direction in similar grid fashion is required to further analyze anisotropy.

Comparison of three theoretical semivariogram models (i.e., spherical, exponential, Whittle or Matern with k=1) revealed that there was no obvious best fitted model to describe the experimental semivariogram of dense gridded measurements. A nested model with an anisotropy ratio helps in estimating the values at unsampled locations with consideration of the correlation of data sampled at different locations. However, for the cases analyzed in this study, the isotropic or omnidirectional semivariogram model can work as well as an anisotropic semivariogram model in estimating the values at unsampled locations. Correctly calculating the experimental semivariogram (i.e., selection of appropriate separation distances and bin sizes) is more important than looking at minor differences between the different models.

Comparisons of directional semivariogram models from dense and sparse datasets from same project are also provided in this report. The summarized spatial variability characteristics showed range values between 2 m and 11 m for dense gridded datasets taken over a relatively small area versus range values between 15 m to 45 m for sparse datasets taken over relatively large areas. Longer ranges represent more spatially continuous data with longer correlation lengths than shorter ranges. The longer ranges in the sparse dataset compared to shorter ranges calculated using the dense grid dataset suggests that there is a nested structure in the data with both short and long range spatial continuity of the measured properties.

Collecting in situ point test measurements in dense grid pattern (with < 1 m separation distance between test points) over long distances is a significant effort. Properly calibrated roller-integrated intelligent compaction measurements that provide virtually 100% coverage of the pavement foundation layer properties can be an excellent data source to properly analyze and assess spatial variability and anisotropy aspects in the future.

# CHAPTER 1. INTRODUCTION

Non-uniform support conditions under pavements can have detrimental effects on the service life of pavements. According to the American Concrete Pavement Association (ACPA), uniformity of the subgrade and subbase layers is more important than the strength of those layers itself (ACPA 2008). White et al. (2004) demonstrated from site characterization and modeling, that the benefits of uniformity of the subgrade support for concrete pavements are evidenced by the reduction of the maximum deflections and principal stresses in the pavement layer. Based on field studies conducted as part of this project and pavement modeling, Brand et al. (2014) states that "non-uniform subgrade support is a complex interaction between the k-value range, the magnitude of k-values, the distribution of the support stiffness relative to the critical loading location, and the size of the predefined area".

Generally, pavement design considers the foundation as a layered medium with uniform material properties and support conditions. But in reality, soil engineering parameters generally show significant spatial variation. Spatial variation of pavement foundation layer support conditions are documented previously by Vennapusa (2004) and White et al. (2004), and also in several of the field studies documented in this project. Better understanding the influence of spatial variability on the performance of geotechnical structures is increasingly being studied for a wide range of geotechnical applications (e.g., Mostyn and Li 1993, Phoon et al. 2000, White et al. 2004, Griffiths et al. 2006). One challenge in this area has been collecting enough information to make use of geostatistics.

Univariate statistical parameters such as the standard deviation and coefficient of variation are often used to assess variability, but they do not properly address the issue of spatial non-uniformity. Two datasets with identical frequency distributions can have significantly different spatial characteristics. Geostatistical analysis tools such as semivariograms can be useful is assessing and modeling the spatial non-uniformity. Also, semivariograms can be used to assess anisotropic conditions, that define variability in longitudinal versus transverse directions relative to the alignment, which can provide insights into influence of the construction methods and its impact on the spatial non-uniformity.

As part of this project, field testing was conducted at several pavement foundation construction sites in a dense grid pattern with relatively close spacing (i.e., < 1 m) over a small area and in a sparse sampling pattern over a large area. The goal was to collect different foundation support characteristics (i.e., moisture content, dry density, strength, and stiffness) and assess their spatial variability. Detailed results of the test measurements and their analysis are presented in the individual project reports prepared as part of this project. In this report, results from selected field studies were analyzed for a more in-depth analysis of spatial variability and assess anisotropy in the different measurements. The measurement parameters assessed include elastic modulus determined from the light weight deflectometer (LWD) test ($E_{LWD-Z3}$), dynamic cone penetration index (DCPI) of subbase layer and subgrade layers ($DCPI_{subbase}$, and $DCPI_{subgrade}$) using dynamic cone penetrometer (DCP) test, and dry unit weight ($\gamma_d$) and moisture content ($w$) determined from the nuclear gauge (NG) test method.

This report contains five chapters. Chapter 2 provides an overview of the in situ testing methods of the results presented in this report and the statistical analysis methods used in this report. Chapter 3 provides an overview of the selected test sections used for analysis in this report. Chapter 4 presents results and analysis of the test results. Chapter 5 presents key findings and conclusions from this report.

The findings from this report should be of significant interest to researchers, practitioners, and agencies who deal with design, construction, and maintenance aspects of PCC pavements. This report is one of several project reports developed as part of the TPF-5(183) and FHWA DTFH 61-06-H-00011:WO18 studies.

# CHAPTER 2. TESTING AND ANALYSIS METHODS

## In Situ Testing Methods

The following in situ testing methods and procedures were used in this study: real-time kinematic (RTK) global positioning system (GPS); Kuab falling weight deflectometer (FWD) setup with 300 mm diameter plate; Zorn light weight deflectometer (LWD) setup with 300 mm diameter plate; dynamic cone penetrometer (DCP); calibrated Humboldt nuclear gauge (NG). Pictures of these test devices are shown in Figure 1.



**Figure 1. Trimble SPS-881 hand-held receiver, Kuab falling weight deflectometer, and Zorn light weight deflectometer (top left to right); dynamic cone penetrometer, nuclear gauge, and nuclear gauge (bottom left to right)**

*Real-Time Kinematic Global Positioning System*

RTK-GPS system was used to obtain spatial coordinates (x, y, and z) of in situ test locations and tested pavement slabs. A Trimble SPS 881 receiver was used with base station correction provided from a Trimble SPS851 established on site. According to the manufacturer, this survey system is capable of horizontal accuracies of < 10 mm and vertical accuracies < 20 mm.

*Zorn Light Weight Deflectometer*

Zorn LWD tests were performed on base and subbase layers to determine elastic modulus. The LWD was setup with 300 mm diameter plate and 71 cm drop height. The tests were performed following manufacturer recommendations (Zorn 2003) and the elastic modulus values were determined using Equation 1:

$$E = \frac{(1 - \eta^2)\sigma_0 r}{D_0} \times F \tag{1}$$

where E = elastic modulus (MPa); $D_0$ = measured deflection under the plate (mm); $\eta$ = Poisson's ratio (0.4); $\sigma_0$ = applied stress (MPa); $r$ = radius of the plate (mm); and F = shape factor depending on stress distribution (assumed as 8/3) (see Vennapusa and White 2009).

The results are reported as $E_{LWD-Z3}$ where Z represents Zorn LWD and 3 represents 300 mm diameter plate.

*Kuab Falling Weight Deflectometer*

Kuab FWD tests on this project were conducted on the CTB base layer. Tests were conducted by applying one seating drop using a nominal force of about 24.5 kN (5500 lb) followed by two test drops, each at a nominal force of about 24.5 kN (5500 lb) and 36.9 kN (8300 lb). The actual applied force was recorded using a load cell. Deflections were recorded using seismometers mounted on the device, per ASTM D4694-09 *Standard Test Method for Deflections with a Falling-Weight-Type Impulse Load Device.*

A composite modulus value ($E_{FWD-K3}$) was calculated using the measured deflection at the center of the plate ($D_0$), corresponding applied contact force, and Equation 1. The plate that used the Kuab FWD is a four-segmented plate, and therefore, shape factor F = 2 was used in the calculations assuming a uniform stress distribution (see Vennapusa and White 2009).

4

*Dynamic Cone Penetrometer*

DCP tests were performed in accordance with ASTM D6951-03 *"Standard Test Method for Use of the Dynamic Cone Penetrometer in Shallow Pavement Applications"* to determine dynamic penetration index (DPI) and calculate California bearing ratio (CBR) using Equation 2.

$$CBR = \frac{292}{DPI^{1.12}}$$  (2)

The DCP test results are presented in this report as CBR with depth profiles at a test location and as point values of DCP-CBR$_{Subbase}$ or DCP-CBR$_{Subgrade}$. The point data values represent the weighted average CBR within each layer. The depths of each layer were identified using the DCP-CBR profiles.

*Nuclear Gauge*

A calibrated nuclear moisture-density gauge (NG) device was used to provide rapid measurements of soil dry unit weight ($\gamma_d$) and moisture content ($w$) in the base materials. Tests were performed following ASTM D6938-10 *"Standard Test Method for In-Place Density and Water Content of Soil and Soil-Aggregate by Nuclear Methods (Shallow Depth)."* Measurements of $w$ and $\gamma_d$ were obtained at each test location, and the average value is reported.

**Univariate Statistical Analysis Methods**

Univariate statistics are used in this study to quantify the variability of pavement foundation properties as determined using limited in-situ tests. Coefficient of variation (COV) values are used in this study as the primary way of quantifying the variability with respect to the mean of the sample. The ratio of standard deviation ($\sigma$) to mean ($\mu$) in Eq. 3 is the COV where $\sigma$ is calculated as Eq. 4 where n is the number of data values, x.

$$COV = \frac{\sigma}{\mu}$$  (3)

$$\sigma = \sqrt{\frac{\sum(x-\mu)^2}{n-1}} \quad \text{and} \quad \mu = \frac{\sum x}{n}$$  (4)

**Spatial Variability Analysis Methods**

*Overview*

Spatial analysis of pavement foundation properties was performed using the statistical analysis program R (see Bivand et al. 2013; Pebesma 2001). The R program calculates the experimental semivariogram efficiently, fits a theoretical semivariogram model with an established statistical

criteria to obtain the best fit to the calculated semivariogram values, and uses ordinary kriging to visualize the fitted semivariogram prediction results over the studied area. The basic steps are summarized below:

- Calculate the omnidirectional experimental semivariogram values with adjustment on lag distance (h), angle tolerance ($\Delta\theta$), and the maximum distance.
- Plot the variogram map as a preliminary study of anisotropy of the experimental semivariogram values of the studied variable.
- Calculate the semivariogram values in four major directions with azimuth angle ($\theta$) is equal to 0°, 45°, 90°, 135° separately to identify existence and type of anisotropy (geometric, zonal, or both), and investigate major and minor anisotropy directions that are generally perpendicular to each other.
- Fit a theoretical model to the omnidirectional experimental semivariogram if isotropic or directional semivariogram if anisotropy is identified, and record values of a, $C_0$, $C_s$ and sum of square errors (SSErr).
- Perform cross-validation with the fitted semivariogram model and calculate the mean square of the prediction error (MSPE).
- Use ordinary kriging with the fitted model to predict the values at unsampled locations among the sampled points and use contour plotting to present the results.

*Semivariogram Modeling Approach*

The calculation of an omnidirectional semivariogram is useful in starting the spatial analysis for investigating the distance parameters to produce a clearer structure without having insufficient bins or amount of data pairs in each bin. The omnidirectional semivariogram can indicate an erratic directional variogram when it exists. Several tolerances ($\Delta\theta$) should be tried to use the smallest tolerance value that still provide good results (Isaaks and Srivastava 1989). The R program allows fitting theoretical semivariograms with a weighted least square method that can provide a better statistically fitted model and allow comparison between different theoretical models.

The maximum cutoff length is controlled to be within 1/3 to ½ of the maximum distance of the studied area to exclude the effect of fewer data pairs at larger separation distances. Figure 2 shows an example of a calculating experimental semivariogram of $E_{LWD-Z3}$ calculated from LWD tests performed on MI I-94 TS1b. The example shows fewer data pairs were obtained with increasing separation distances, the variance of the semivariogram values is larger at larger separation distance, and semivariogram values start to decrease at about 2/3 of the maximum distance of the studied area when number of data pairs is smaller.

Extreme values or outliers should be identified and removed before calculating the experimental semivariogram, because the semivariogram values are sensitive to these extreme values that can introduce errors in studying the spatial continuity. For illustration, a bubble plot of DCPI values is shown in Figure 3, which is helpful in locating the extreme values. In this case at test point with 22.6 mm/blow DCPI value is considered an outlier.
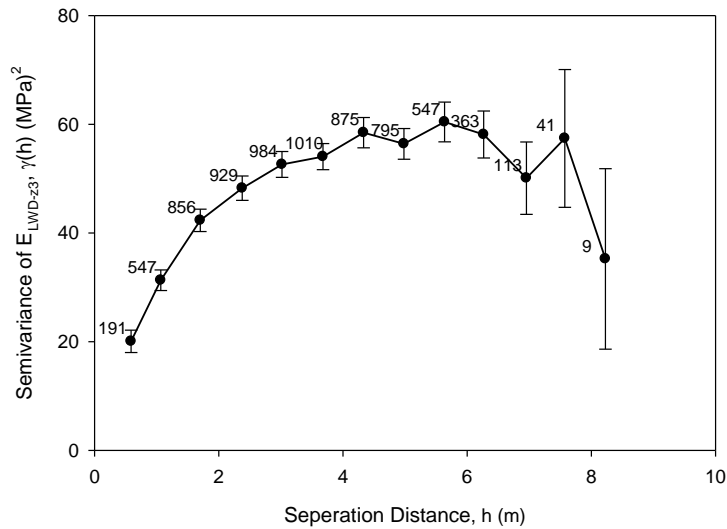
**Figure 2. Illustration of choosing the maximum cutoff length (MI I-94 TS1b)**
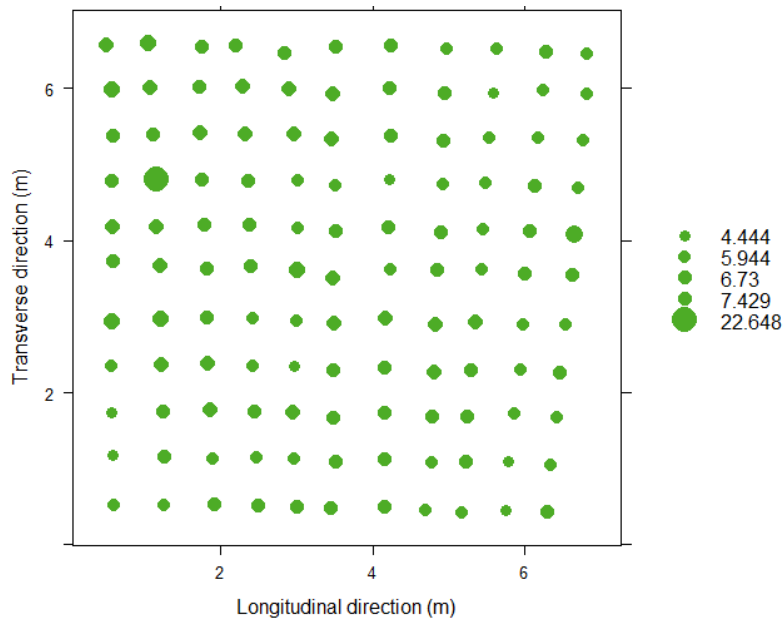


**Figure 3. Bubble plot of DCPI values of subbase layer**

Although the experimental semivariogram summarizes the mean semivariogram for each lag distance (h), it does not give the value of correlation length that should be obtained by fitting the theoretical semivariogram models. The most important characteristic for the choice of the variogram model is the interpretation of the behavior at the origin. The objective of fitting a theoretical semivariogram models to the experimental semivariogram is to capture the major spatial features of the studied variable (Goovaerts 1997). Webster and Oliver (2007) summarized several semivariogram models and there are selected model types is summarized in Table 1.

**Table 1. Summary of different semivariogram models**

| Model | R code | Equation | Parameter note |
|---|---|---|---|
| Nugget | Nug | $\hat{\gamma}(h)=\begin{cases}0 & h=0 \\ C_0 & h\neq 0\end{cases}$ | |
| Spherical | Sph | $\hat{\gamma}(h)=\begin{cases}C_s\left(\dfrac{3}{2}\dfrac{h}{r}-\dfrac{1}{2}\left(\dfrac{h}{r}\right)^3\right) & 0\leq h\leq r \\ C_s & h>r\end{cases}$ | a = *r* (range reaches 100% of $C_s$) |
| Gaussian (Matérn, *k*=∞) | Gau | $\hat{\gamma}(h)=\begin{cases}0 & h=0 \\ C_s\left(1-e^{-\left(\frac{h}{r}\right)^2}\right) & h>0\end{cases}$ | a′ = $\sqrt{3}r$ (effective range reaches 95% of $C_s$) |
| Exponential (Matérn, *k*=0.5) | Exp | $\hat{\gamma}(h)=\begin{cases}0 & h=0 \\ C_s\left(1-e^{-\frac{h}{r}}\right) & h>0\end{cases}$ | a′ = 3*r* (effective range reaches 95% of $C_s$) |
| Whittles (Matérn, *k*=1) | Bes | $\hat{\gamma}(h)=\begin{cases}0 & h=0 \\ C_s\left(1-\left(\dfrac{h}{r}\right)K_1\left(\dfrac{h}{r}\right)\right) & h>0\end{cases}$ | a′ = 4*r* (effective range reaches 95% of $C_s$) |
| Matérn | Mat | $\hat{\gamma}(h)=\begin{cases}0 & h=0 \\ C_s\left(1-\dfrac{1}{2^{k-1}\Gamma(k)}\left(\dfrac{h}{r}\right)^k K_k\left(\dfrac{h}{r}\right)\right) & h>0\end{cases}$ | *k* (smoothness parameter) |

Note: $\Gamma(k)$ and $K_k(h/r)$ are Gamma function and modified Bessel function of the second kind with order *k* respectively, *r* is the range parameter obtained in R program.

Goovaerts (1997) suggested that models with parabolic behavior at the origin (i.e., Gaussian model) should be used for highly continuous properties (i.e., ground water levels). The Gaussian model is not suggested (Wackernagel 2003; Webster and Oliver 2007) for describing the spatial variability of general properties that are not highly continuous. Pavement foundation properties are not be expected to be highly continuous variable, so a Gaussian model will be not be used in this paper.

In this report, application of a spherical (Sph) model, an exponential (Exp) model, and Matérn (Mat, *k*=1) models in describing spatial variability of pavement foundation properties.

The Matérn model class has a smoothness parameter (*k*) to describe the behavior of the semivariogram at the origin. The exponential model, Whittle's model, and Gaussian model are particular cases of the Matérn model with *k* equal to 0.5, 1, and infinity, respectively. With *k*=∞ the Gaussian model describes the most continuous origin behavior.

An experimental semivariogram is meaningless with only a pure nugget effect model fitted that indicates the studied properties lack spatial continuity within the studied area (Olea 2006). Therefore, the nugget model is generally nested with other models. Nested models are combinations of different models where properties of the original models are not changed. There are many possible combinations of semivariogram models. A combination of basic models is

generally required to satisfactorily fit the directional experimental semivariogram, but overfitting the semivariogram with complicated a model that consists of three or more basic models usually will not result in more accurate estimates than using the simpler models.

Olea (2006) reported that nested models are often a combination of two simple models and one pure nugget effect model as shown in Eq. 5.

$$\hat{\gamma}(h) = \sum_{i=0}^{k} C_0 + C_i \gamma_i(h) \tag{5}$$

Equation 6 shows a nested model consisting of a nugget effect model, an exponential model, and a Gaussian model:

$$\hat{\gamma}(h) = \begin{cases} 0 & h=0 \\ C_0 + C_{s1}\left(\frac{3}{2}\frac{h}{a_1} - \frac{1}{2}\left(\frac{h}{a_1}\right)^3\right) + C_{s2}\left(1 - e^{-3\left(\frac{h}{a_2}\right)}\right) & h \neq 0 \end{cases} \tag{6}$$

Figure 4 shows semivariogram plots of these four models with values assigned to C and a and a′ where sill = 1.
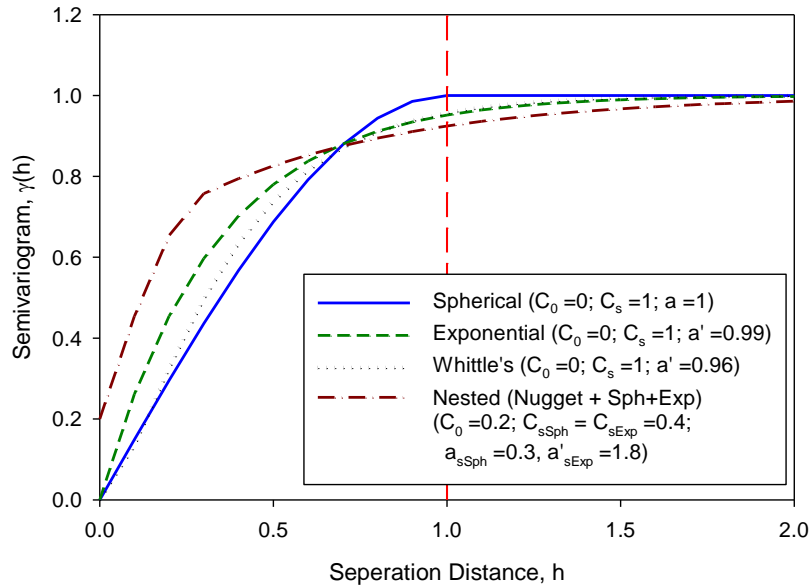


**Figure 4. Sample semivariogram plots of spherical, exponential, Gaussian, and nested models with values assigned to C and a and a′ where sill = 1**

*Model Selection*

The theoretical model can be fit to the experimental semivariogram to describe the spatial variability of the data with quantified parameters. The theoretical model can be selected based on

9

one of two methods; one method chooses the model that best fits the calculated experimental semivariogram values, another method chooses the model that gives the best predictions. Four statistical criteria are discussed here. Three methods for defining the "best fit" use either the squared errors (SSErr), Akaike information criterion (AIC), or Cressie goodness of fit (GoF). The mean squares prediction error (MSPE) can be used to choose the model that give the "best" predictions.

Fitting a semivariogram model by eye relies on the averaged semivariance values at each lag distance and ignores the number of pairs of data spaced at that lag distance. A weighted least squares method as Cressie (1985) suggested will be used for this study. The weighted least squares method gives the most weight to the early lags and less weight to those lags that have fewer data pairs. Therefore, the weighted least squares method allows fitting the theoretical model to capture the major spatial characteristics of the variable, rather than not to be the closest to the experimental values.

There are several methods for calculating the weight ($w_i$) for the weighted least squares fit, the weight calculation method used in this study is presented in Eq. 7 with $N_i$ is the number of data pairs that are separated by a distance $h_i$.

$$w_i = \frac{N_i}{h_i^2} \tag{7}$$

In this study, exponential, spherical, and Matérn ($k=1$) modelS are fitted to the experimental semivariogram and the nested model of more than one structure might be used to better describe the anisotropic experimental semivariogram. The sum of square errors (SSErr) is calculated for each fitted theoretical semivariogram to describe how well the model fits the experimental semivariogram. In calculation of SSErr (Eq. 8), $\hat{\gamma}(h_j)$ is the predicted semivariogram value with the fitted theoretical model and $\gamma(h_i)$ is the average experimental semivariogram value at a set of lag distance $h_i$.

$$SSErr = \sum_{i=1}^{n} w_i [\hat{\gamma}(h_i) - \gamma(h_i)]^2 \tag{8}$$

Equation 9 is used to calculate AIC (Jian et al. 1996; Webster and Oliver 2007) where n is the number of experimental semivariogram values and $p$ is the number of parameters in that theoretical model. Since the three models (i.e., spherical, exponential, Matérn with $k=1$) have the same $p$ is equal to three, using the AIC criteria is not different from using SSErr.

$$\widehat{AIC} = n \ln \left( \frac{SSErr}{n} \right) + 2p \tag{9}$$

Clark and Harper (2002) suggested a modified Cressie goodness of fit (GoF) criteria to measure how well the model fits the data. Smaller GoF indicates better fit of the theoretical semivariogram model to the experimental semivariogram values. GoF is calculated with Eq. 10,

where $N_h$ is the number of data pairs used to calculate the average experimental semivariogram $\gamma(h)$ at lag or separation distance h, and $\hat{\gamma}(h)$ is the fitted theoretical semivariogram at h.

$$GoF = \frac{1}{\sum_h N_h} \sum_h N_h \left(\frac{\hat{\gamma}(h)-\gamma(h)}{\gamma(h)}\right)^2 \tag{10}$$

SSErr, AIC and GoF are used to measure how well the theoretical model fits the experimental semivariogram values. However, they may not measure the goodness of using the fitted model to describe the spatial variability of the studied variable. Therefore, the mean squared prediction error (MSPE) using the fitted model to predict the variable values at unsampled locations, calculated from cross-validation, can be used to evaluate the better semivariogram model for that variable.

The objective of fitting the experimental semivariogram is to describe the spatial continuity of the studied variable and ultimately to estimate the variable values at the unsampled locations. The impacts of different models on interpolating experimental semivariogram results can be compared through cross-validation (Isaaks and Srivastava 1989). The cross-validation process involves removing the first data value $Z(\mathbf{s}_i)$ at location $\mathbf{s}_i$ (i=1 to N) and using the rest (N-1) of the data values sampled over the study area to fit the theoretical semivariogram model and predicted $\hat{Z}(\mathbf{s}_i)$ and calculating the squared error for the first data value. The cross-validation process is repeated for all data values sampled at all N locations $\mathbf{s}_i$, and the average squared error in the cross-validation process is calculated as the mean squared prediction error (MSPE) in Eq. 11.

$$MSPE = \frac{1}{N}\left[Z(\mathbf{s}_i) - \hat{Z}(\mathbf{s}_i)\right]^2 \tag{11}$$

The basic idea of cross validation is removing one data point at a time from the data set and re-estimating this value from the remaining data using the different semivariogram models. Interpolated and actual values are compared, and the model that yields the most accurate predictions is retained.

*Anisotropy in Semivariogram Modeling*

Anisotropy is the phenomenon that the spatial variability is a function of the magnitude and the direction of the separation distance vector $\mathbf{h}$. Two types of two-dimensional anisotropy are defined as geometric anisotropy and zonal anisotropy (Goovaerts 1997) and shown in Figure 4. Eriksson and Siska (2000) clarified the details in calculations of modelling anisotropy in spatial analysis with defining the types of anisotropy to be nugget anisotropy, range anisotropy, and sill anisotropy. Isaaks and Srivastava (1989) and Goovaerts (1997) presented the concept of geometric and zonal anisotropy in spatial analysis.

Geometric anisotropy can be identified when the directional semivariograms have the same shape and sill values ($C_0$ and $C_s$) but different range values and the rose diagram or plot of range values versus the azimuth $\theta$ of the direction is an ellipse (Goovaerts 1997). Azimuth angle $\theta$ is

counted clockwise from the north. The anisotropy ratio ($\lambda<1$) is the ratio of the minor range ($a_\phi$) to the major range ($a_\delta$) of the directional semivariograms that are generally perpendicular to each other. Zonal anisotropy can be identified when the directional semivariograms have different partial sill values.
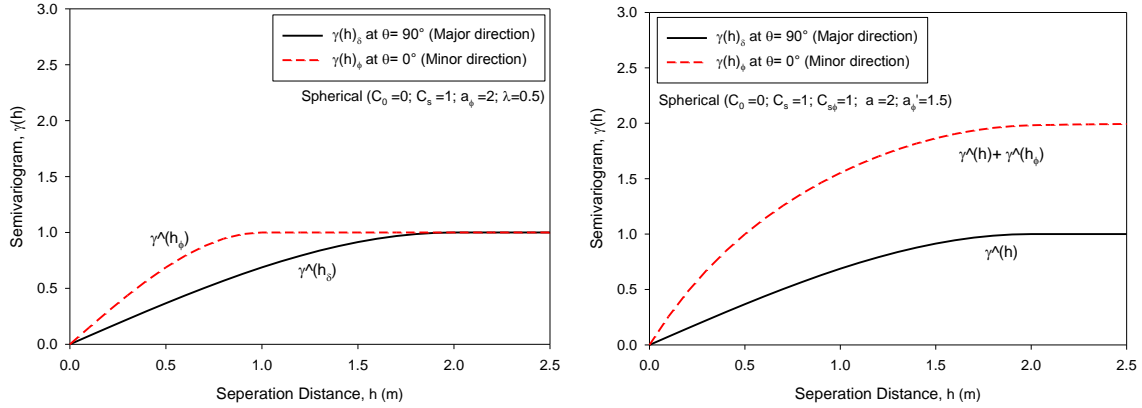


**Figure 5. Types of anisotropy: (a) geometric anisotropy; (b) zonal anisotropy**

Geometric anisotropic semivariogram can be modeled by rotating the coordinate system clockwise to make the major direction ($\delta$) that has the longer range to be aligned with an axis and rescale the anisotropic range to be the minor range $a_\phi$ (Eq. 12).

$$\gamma(\boldsymbol{h}) = \gamma(\boldsymbol{h}^*) \quad \text{with} \quad \boldsymbol{h}^* = \begin{bmatrix} 1 & 0 \\ 0 & \lambda \end{bmatrix} \begin{bmatrix} cos\delta & -sin\delta \\ sin\delta & cos\delta \end{bmatrix} \boldsymbol{h} \tag{12}$$

Zonal anisotropic semivariogram can be modeled by clockwise rotating the coordinate system to have the direction that shows the maximum continuity (lowest $C_s$) aligned with an axis and set the range ($a_\delta$) in that direction to be a very large value towards infinity ($\lambda$ is very small towards zero) (Eq. 13).

$$\gamma(\boldsymbol{h}) = \gamma_1(\mathrm{h}) + \gamma_2(\boldsymbol{h}^*) \quad \text{with} \quad \boldsymbol{h}^* = \begin{bmatrix} 1 & 0 \\ 0 & 0 \end{bmatrix} \begin{bmatrix} cos\delta & -sin\delta \\ sin\delta & cos\delta \end{bmatrix} \boldsymbol{h} \tag{13}$$

Semivariogram maps (Goovaerts 1997; Isaaks and Srivastava 1989) can be used as a tool that can detect anisotropy directions. The computation of a semivariogram map requires considering many directions and lags. A semivariogram map can be a useful tool in the preliminary study of the major and minor spatial continuity directions. However, the spatial resolution of the semivariogram map will be largely reduced when sparse and irregular spaced data are collected (Facas et al. 2010). Figure 6 shows the process of plotting the semivariogram map and also shows semivariogram values are the same in the opposite direction.
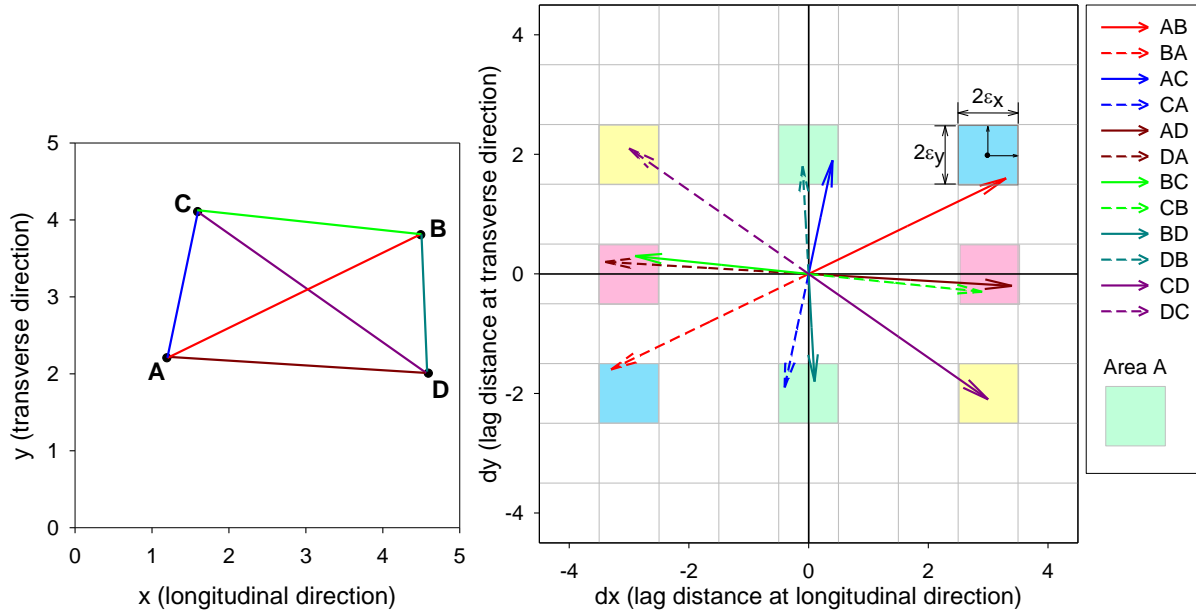
**Figure 6. Methodology of plotting a semivariogram map**

*Kriging*

Kriging is a popular contouring method that is used to estimate the value at unsampled locations. The word kriging means optimal prediction (Cressie 1993). Kriging is used to make prediction on values of a continuous variable Z at unsampled locations using the observed value at sampled locations of the study area. Kriging makes no distributional assumptions and the variates are statistically correlated. Ordinary kriging and the minimum mean squared prediction error will be used in this study to present the fitted semivariogram model. The two assumptions in ordinary kriging are that the local mean is unknown but constant and the sum of the coefficients of the linear predictor is equal to one. The assumptions guarantee that the mean of the predicted values is the same as the observed values over the study area (Cressie 1993; Goovaerts 1997; Journel and Huijbregts 1978). The brief description of ordinary kriging is only to introduce the basics of understanding how the kriged contour map is created. The ordinary kriging estimator $Z_{OK}^{*}(\mathbf{s})$ at location $\mathbf{s}$ is written as a linear combination of the $n(s)$ random variables $Z(\mathbf{s}_i)$ with the kriging weights forced to be equal to 1 (Eq. 14).

$$Z_{OK}^{*}(\mathbf{s}) = \sum_{i=1}^{n(\mathbf{s})} \varepsilon_i^{OK}(\mathbf{s}) Z(\mathbf{s}_i) \quad \text{with} \quad \sum_{i=1}^{n(\mathbf{s})} \varepsilon_i^{OK}(\mathbf{s}) = 1 \tag{14}$$

13

# CHAPTER 3. TEST SECTIONS

This chapter presents brief background information of each project discussed in this report along with the test section details. Detailed information of the field projects is provided in the respective field project reports.

## Michigan I-94 Project Test Sections

This project is located on I-94 in St. Clair and Macomb Counties, Michigan. The project involved reconstruction of pavement foundation layers of the existing interstate highway between about mile posts 23.6 and 6.1 (about Station 794+12 to 1121+70; Michigan Project No. IM0877(023) and Job Number 100701A). The new PCC pavement was constructed with nominal 280 mm (11 in.) thickness. During the reconstruction, the existing pavements were removed and the foundation layers were undercut to a depth of about 690 mm (27 in.) below the existing pavement surface elevation for placement of the open graded drainage course (OGDC) base layer with a geotextile separation layer at the interface.

Results from two test sections from this field project are presented in this report (TS1 and TS3). Both these sections consisted of compacted newly constructed OGDC base layer. Summary information from these test sections are presented in Table 2.

**Table 2. Summary of test sections and in situ testing – MI I-94 Project**

| TS | Date | Location | Material | In situ Test Measurements | Comments |
|---|---|---|---|---|---|
| 1a | 5/27/2009 | Sta. 804+00 to 813+00 [I-94 EB] | Newly constructed base | NG, DCP, LWD | Section tested after trimmed to grade. |
| 1b | 5/28/2009 | Sta. 809+00 [I-94 EB] (7 m x 7 m area) | Newly constructed base | NG, DCP, LWD | Section tested after trimmed to grade. Testing was performed in 0.6 m x 0.6 m grid. |
| 3a | 5/28/2009 | Sta. 839+50 to 866+00 | Newly constructed base | DCP, LWD, FWD, PLT | Section tested prior to trimming. |

TS1 involved testing the OGDC base layer on I-94 EB lanes between Sta. 804+00 and 813+00. The material was placed, compacted, and trimmed in this area prior to our testing. TS1a involved testing every +50 station between Sta. 804+00 and 813+00 (Figure 8) along the centerline of the I-94 EB alignment and left and right of the centerline at about 4 m offsets, representing a sparse systematic sampling method. TS1b involved testing a 7 m x 7 m area near Sta. 809+00 in a dense grid pattern (Figure 8) with 121 test points. NG, LWD, GPT, and DCP tests were conducted on this test section.
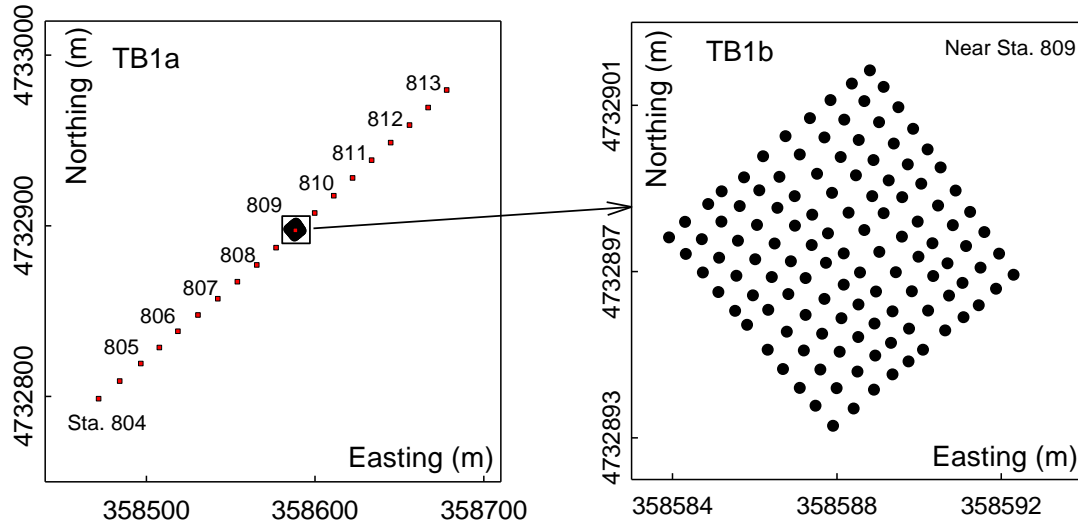
**Figure 7. MI I-94 TS1: Plan view of in situ test locations**



**Figure 8. MI I-94 TS1b: Photograph showing testing on the 0.6 m x 0.6 m grid pattern**

TS3a involved testing the OGDC base layer between Sta. 839+50 and 890+00. The material was placed and compacted in this area prior to our testing, but was not trimmed to the final grade. TS3a involved testing using point measurements at every +50 station between Sta. 839+50 and 866+00 (Figure 9) along the center line of the I-94 EB alignment, and left and right of the center line at about 4 m offsets, representing sparse systematic sampling. NG, DCP, LWD, and FWD point tests were conducted on TS3a.

15
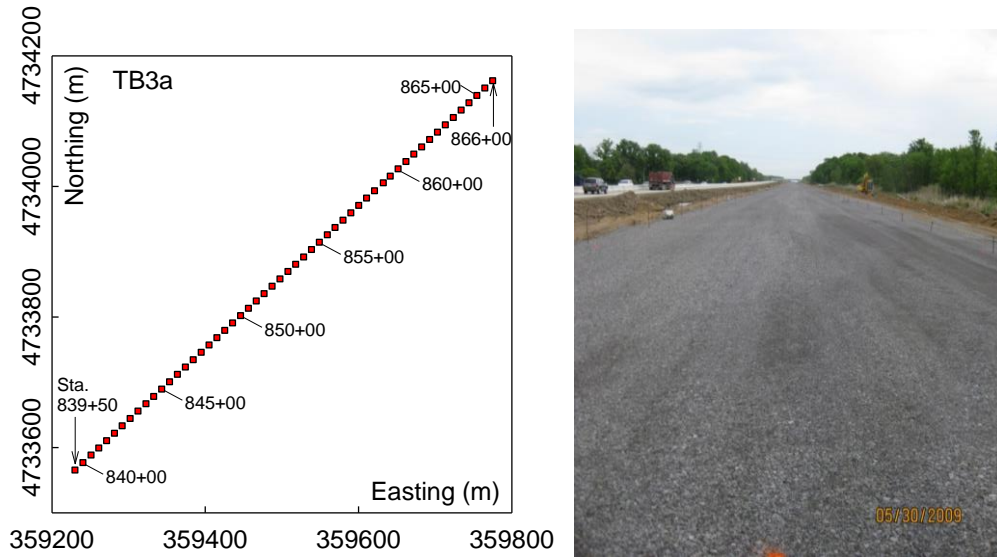
**Figure 9. MI I-94 TS3: Plan view of in situ test locations (left) and photograph of the untrimmed OGDC base layer (right)**

**Michigan I-96 Project Test Sections**

This project involved reconstruction of about 5.8 miles of I-96 from just west of Wacousta Road (mile post 90) to south of M-43 (mile post 93) in Clinton and Eaton Counties near Lansing, Michigan. The pavement structure was reconstructed with a twenty-year design life jointed PCC pavement that was composed of a 292 mm (11.5 in.) thick PCC pavement at 4.3 m (14 ft) joint spacing, a 127 mm (5 in.) cement treated base (CTB) layer with recycled PCC (RPCC) material and a 279 mm (11 in.) existing or new sand subbase with a geotextile separator at the CTB/subbase interface.

Results from three test sections from this field project are presented in this report (TS1 to TS3). Two of these sections consisted sand subbase layer underlain by subgrade and one of the sections consisted of CTB layer. Summary information from these test sections are presented in Table 3.

TS1 and TS3 consisted of testing the final compacted and trimmed sand subbase layer along I-96 EB lane alignment with NG, LWD, and DCP. TS3 involved testing between Sta. 458+00 and 468+50 at every +50 station along the centerline of the alignment, representing a sparse systematic sampling method. In addition, tests were conducted at five test locations across the pavement width at Sta. 461+50. TS1 involved testing a 9 m x 9 m area near Sta. 464+40 in a dense grid pattern with 73 test points. A plan layout with GPS coordinates of the test locations on TS1 and TS3 are shown in Figure 9.

TS2 consisted of testing the CTB layer along I-96 EB right lane just west of West Grand River Avenue overpass between Sta. 296+00 and 299+00 (Figure 11). NG and FWD tests were conducted in this section. Tests were conducted in a grid pattern with five tests across the lane

and at every 3 m along the alignment over a 90 m long section. NG and FWD tests were conducted at 119 test points.

**Table 3. Summary of test sections and in situ testing – MI I-96 Project**

| TS | Date | Location | Material | In situ Test Measurements | Comments |
|---|---|---|---|---|---|
| 1 | 5/18/10 | Between Hwy M-43 exit ramp and Hwy M-43 overpass on I-96 east/south bound lane (near Sta. 464+40) | Sand subbase layer underlain by subgrade | NG, DCP, LWD | In situ testing at 73 points in a dense grid pattern |
| 2 | 5/19/10 and 5/23/10 | West of W Grand River Avenue overpass on I-96 east/south bound lane (between Sta. 296+00 and 299+00) | CTB underlain by sand subbase and subgrade | FWD, NG | CTB placed on 5/15/10; FWD and NG tests at 119 points |
| 3 | 5/20/10 | Along centerline from Sta. 468+50 to 458+00 near Hwy M-43 on I-96 east/south bound lane | Sand subbase layer underlain by subgrade | NG, DCP, LWD | Additional tests across the width of the pavement base at Sta. 461+50. |
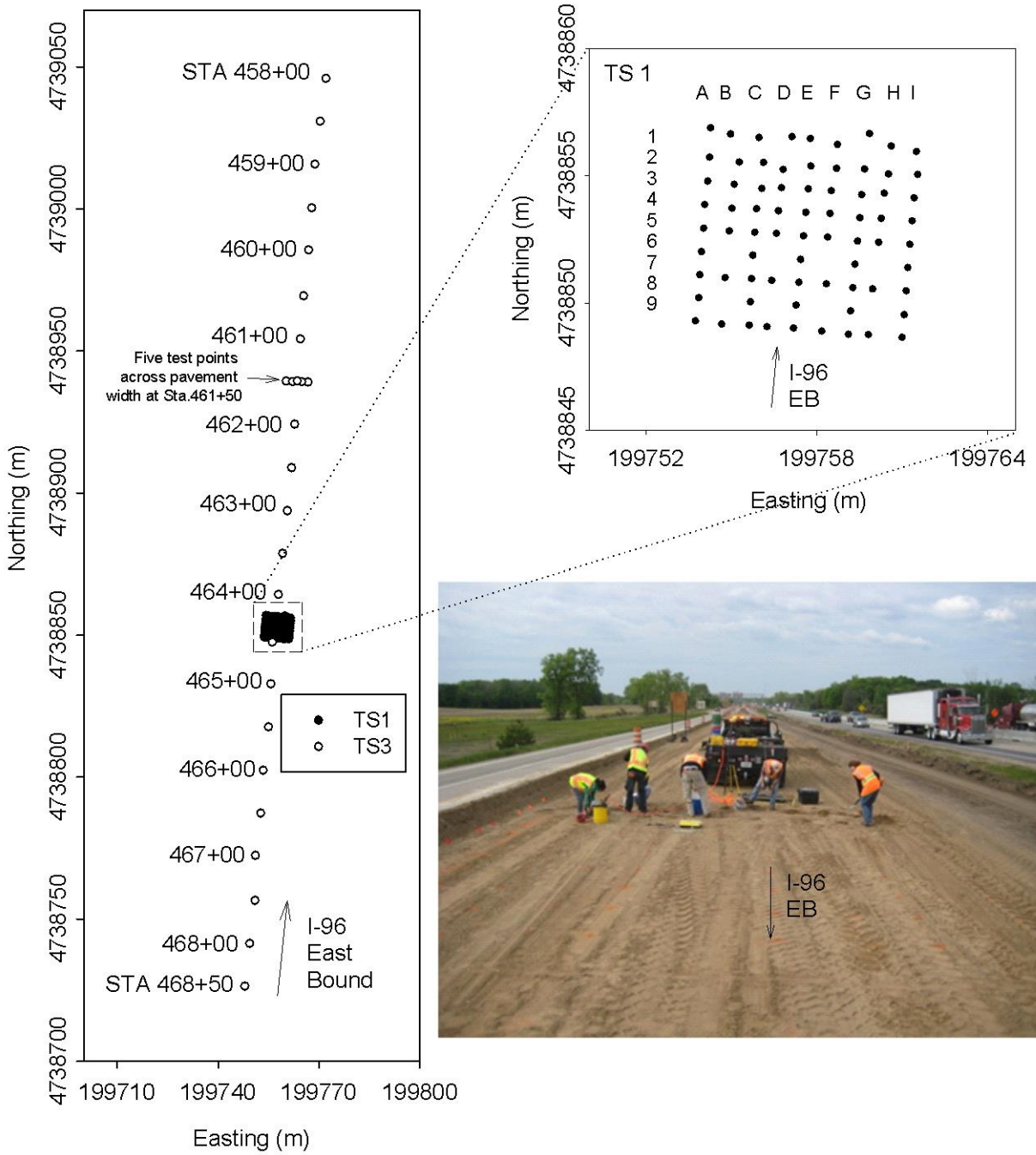
**Figure 10. MI I-96 TS1/TS3: Plan view of in situ test locations (left), detailed plan layout (top right), and image showing test locations**

**Figure 11. MI I-96 TS2 CTB layer (looking east near Sta. 296+25)**

## Wisconsin US10 Test Sections

This project involved new construction of 5.44 miles of US Highway 10 from Sta. 285+50 to Sta. 580+50 in Portage County, Wisconsin. ISU testing was conducted on two test sections located on the east side of County Highway O (TS1) and west side of County Highway G (TS2). Summary of the test sections is provided in Table 4.

TS1 consisted of a relatively loose sand subbase layer placed over the subgrade along US 10WB lane between Sta. 555+00 and 575+00. NG, LWD, and DCP tests.

TS2 consisted of testing the final compacted subgrade layer along US10WB lane near Sta. 495+00. A plan area of about 8 m x 28 m was selected for dense grid testing with about 70 test locations. In addition, tests were conducted every 3 m along the centerline of the alignment over 65 m long stretch of the road. A plan view of the TS with GPS measurements of the test locations is provided in Figure 14. In situ tests on this TS involved LWD, NG, and DCP tests.

**Table 4. Summary of test sections and in situ testing – WI US10 Project**

| TS | Date | Location | Material | In Situ Tests | Comments |
|---|---|---|---|---|---|
| 1 | 5/25/10 | US10WB lane at two locations: TS1: Between Sta. 555+00 and 565+00 | Sandy subbase (loose) underlain by subgrade. Note: Thick sand subbase (~ 600 mm) | NG, DCP, LWD | TS1: Tests performed every 3 m along the centerline of US 10WB lane. In addition, seven tests across pavement width near Sta. 560+00. |
| 2 | 5/24 to 5/25/10 | US10 WB lane West of Co Rd G near Sta. 495+00 | Subgrade | NG, DCP, LWD | 8 m x 28 m dense spatial grid section and tests every 3 m along the centerline of US 10WB |
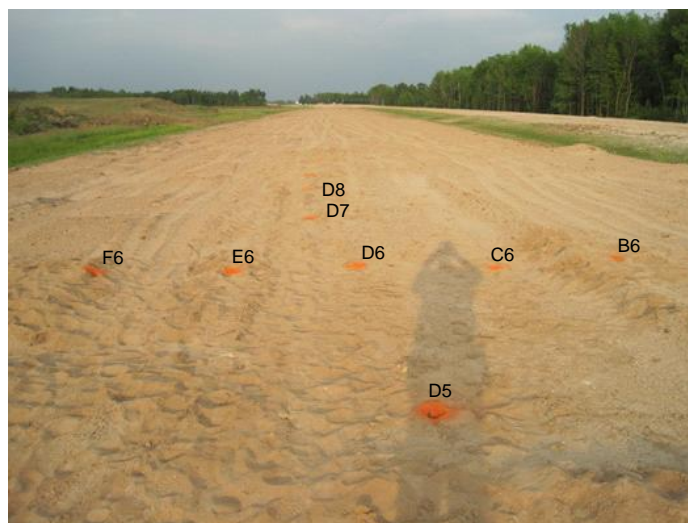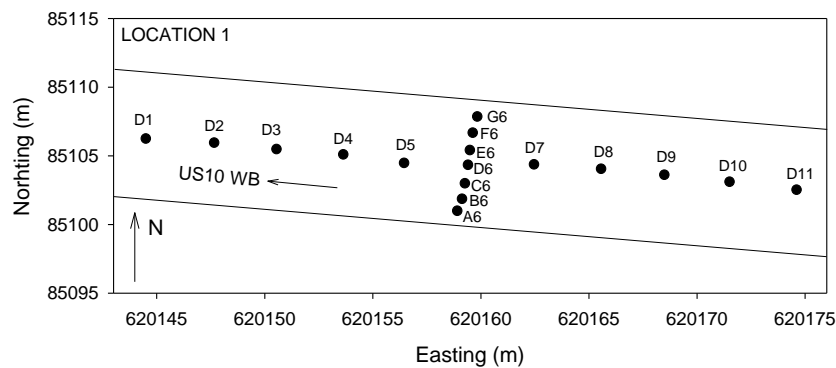


**Figure 12. WI US10 TS1: Plan view (top) and a photo (bottom) of in situ test locations on TS1**

**Figure 13. WI US10 TS2: Photograph of the compacted subgrade**
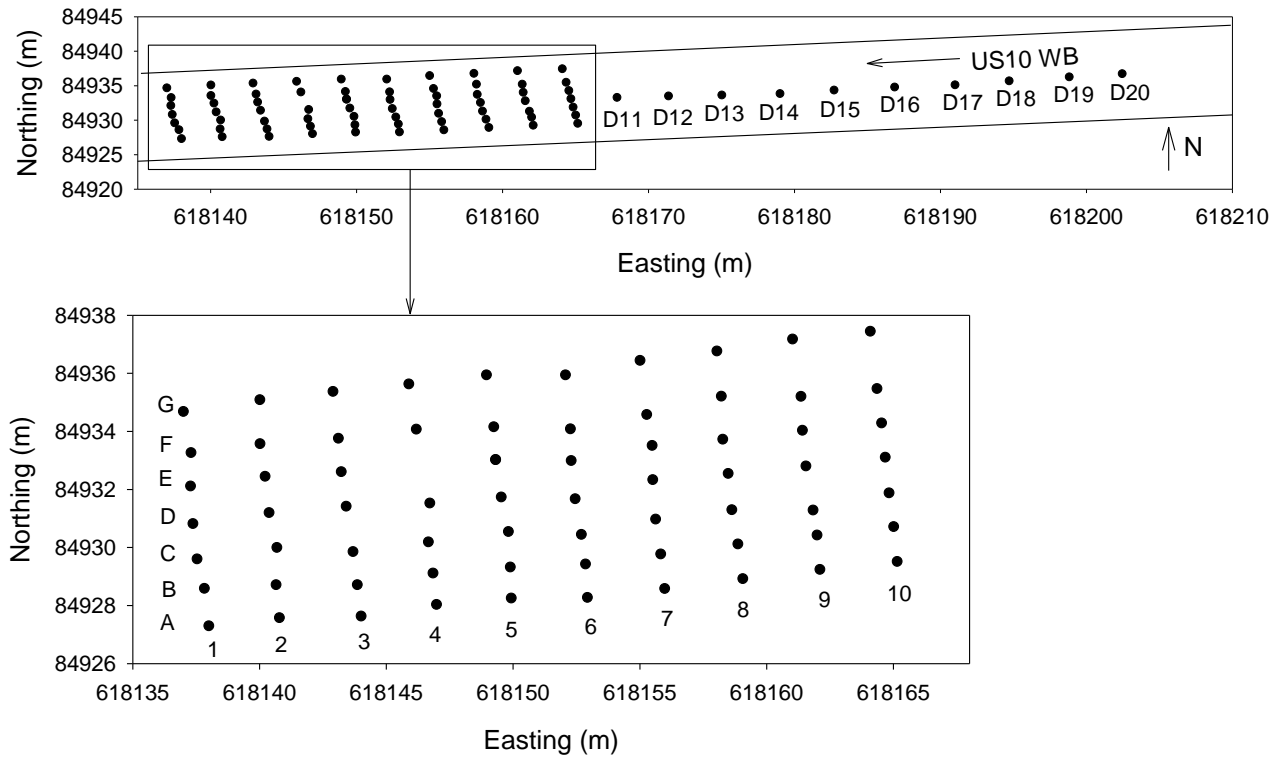


**Figure 14. WI US10 TS2: Plan view of test locations**

**Iowa US30 Test Sections**

This project is located on US 30 in Boone County in Iowa between mileposts 139.0 and 147.27. As part of the reconstruction work that began in summer of 2011, the existing pavement was removed and the subgrade was undercut during the reconstruction process to place a nominal 410 mm (16 in.) thick modified subbase over the natural existing subgrade. The modified subbase layer consisted of 150 mm (6 in.) thick RPCC material at the surface underlain by 260 mm (10 in.) thick mixture of RPCC/RAP material. A nominal 254 mm (10 in.) thick JPCP was placed on the newly constructed foundation layer. DCP and LWD tests were conducted on the RPCC modified subbase layer on August 8, 2011 in 2 test sections along the left and right of the center lane using a sparse systematic sampling approach. Tests were conducted after compaction and trimming operations are completed and just prior to paving operations. All testing was conducted on US30 EB lane near between Sta. 1394+00 and 1396+00.



**Figure 15. IA US30: Field testing on finished RPCC modified subbase layer (June 8, 2011)**

**Summary of All Test Sections**

A summary of all test sections showing the soil index properties of the tested materials, and a summary of the sampling methods used in each section is provided in Tables 4 and 5.

**Table 5. Soil index properties and classification of materials from different test sections**

| Site | Test Section (TS) | Layer | Soil index properties and classification | | | | | |
|---|---|---|---|---|---|---|---|---|
| | | | $\gamma_{dmax}$ $(kN/m^3)^a$ | $\gamma_{dmin}$ $(kN/m^3)^b$ | $\gamma_{dmax}$ $(kN/m^3)^c$ | $W_{opt}$ $(\%)^c$ | AASHTO | USCS |
| MI I-94 | TS1a | Base | 16.23 | 4.05 | — | — | A-1-a | GP |
| | TS1b | Base | 16.23 | 4.05 | — | — | A-1-a | GP |
| | TS3 | Base | 16.23 | 4.05 | — | — | A-1-a | GP |
| MI I-96 | TS1 | Sand subbase | 20.06 | 14.98 | 19.96 | 7.9 | A-1-b | SP-SM |
| | TS2 | CTB | 13.61 | 12.26 | — | — | A-1-a | GP |
| | TS3 | Sand subbase | 20.06 | 14.98 | 19.96 | 7.9 | A-1-b | SP-SM |
| WI US-10 | TS1 | Sandy Subbase | 18.19 | 15.07 | 17.37 | 11.8 | A-3 | SP |
| | TS2 | Subgrade | — | — | 18.67 | 12 | A-6(8) | CL |
| IA US-30 | TS1 | RPCC modified Subbase | — | — | 19.3 | 10.3 | A-1-a | GP-GM |
| | TS2 | RPCC modified Subbase | — | — | 19.3 | 10.3 | A-1-a | GP-GM |

**Table 6. Sampling method and calculated sampling rate from different test sections**

| Site | Test Section (TS) | Sampling rate | | | |
|---|---|---|---|---|---|
| | | Sample grid | Max Length (m) | N of Tests | N/ unit length (N/m) |
| MI I-94 | TS1a | Sparse | 274.3 | 54 | 0.20 |
| | TS1b | Dense | 6.3 | 121 | 19.12 |
| | TS3 | Sparse | 807.9 | 162 | 0.20 |
| MI I-96 | TS1 | Dense | 7.9 | 73 | 9.22 |
| | TS2 | Sparse | 90.7 | 119 | 1.31 |
| | TS3 | Sparse | 320.5 | 26 | 0.08 |
| WI US-10 | TS1 | Sparse | 65.4 | 80 | 1.22 |
| | TS2 | Sparse | 6.9 | 17 | 2.46 |
| IA US-30 | TS1 | Sparse | 106.7 | 20 | 0.19 |
| | TS2 | Sparse | 104.3 | 52 | 0.50 |

# CHAPTER 4. RESULTS AND ANALYSIS

## Univariate Statistical Analysis Results

Univariate statistics are calculated for data measured on each test section from all project sites. The results are presented in Tables 7 to 10. The statistical parameters summarized in these tables included mean, median, variance, standard deviation, COV, and skewness (measure of normal distribution).

Results showed that the COV of moduli and DCP index values ranged between 12% and 39%, COV of moisture content varied between 11% and 25%, and COV of dry density values ranged between 2% and 6%.

**Table 7. Univariate statistics summary of $E_{LWD-Z3}$ (MPa)**

| Field site | TS | Layer | Univariate Statistics | | | | | | | |
|---|---|---|---|---|---|---|---|---|---|---|
| | | | Mean (μ) | Median | Variance ($s^2$) | Std Dev (σ) | COV | N | Skewness |
| MI I-94 | TS1a | Base | 73.3 | 73.7 | 206.0 | 14.4 | 20 | 54 | 0.27 |
| | TS1b | Base | 58.5 | 58.6 | 50.5 | 7.1 | 12 | 121 | 0.43 |
| | TS3 | Base | 49.0 | 49.6 | 109.8 | 10.5 | 21 | 162 | 0.06 |
| MI I-96 | TS1 | Sand subbase | 30.9 | 31.3 | 124.1 | 11.1 | 36 | 73 | -0.20 |
| | TS2 | CTB | 214.8 | 216.9 | 7152.4 | 84.57 | 39 | 119 | 0.29 |
| | TS3 | Sand subbase | 33.2 | 35.8 | 108.7 | 10.4 | 31 | 26 | -0.57 |
| WI US-10 | TS1 | Sandy Subbase | 12.6 | 12.6 | 10.3 | 3.2 | 25 | 17 | 0.00 |
| | TS2 | Subgrade | 30.7 | 30.4 | 28.3 | 5.3 | 17 | 80 | 0.62 |
| IA US-30 | TS2 | RPCC modified Subbase | 56.6 | 57.5 | 120.6 | 11.0 | 19 | 40 | -0.81 |

**Table 8. Univariate statistics summary of other pavement foundation properties**

| Field site | TS | Layer | Properties | Univariate Statistics | | | | | | |
|---|---|---|---|---|---|---|---|---|---|---|
| | | | | Mean ($\mu$) | Median | Variance ($s^2$) | Std Dev ($\sigma$) | COV | N | Skewness |
| MI I-94 | TS1a | Base | DCPI | 6 | 6 | 3.0 | 1.7 | 27 | 54 | 1.87 |
| | TS1b | Base | DCPI | 7 | 7 | 1.3 | 1.1 | 17 | 120 | 0.48 |
| | TS3 | Base | $E_{FWD-k3}$ | 44.7 | 44.4 | 195.0 | 14.0 | 31 | 50 | 0.83 |
| | | | DCPI | 8 | 8 | 3.8 | 2.0 | 23 | 162 | 0.69 |
| MI I-96 | TS1 | Sand subbase | DCPI | 19 | 19 | 20.7 | 4.5 | 24 | 57 | 0.37 |
| | TS3 | Sand subbase | DCPI | 16 | 16 | 25.0 | 5.0 | 30 | 26 | 0.45 |
| WI US10 | TS1 | Sandy Subbase | CBR | 5.6 | 5.7 | 1.4 | 1.2 | 22 | 17 | -1.1 |
| | TS2 | Subgrade | CBR | 15.4 | 14.5 | 24.8 | 5.0 | 32 | 79 | 1.2 |
| IA US30 | TS1 | RPCC Subbase | CBR | 11.0 | 9.6 | 14.9 | 3.9 | 35 | 20 | 1.08 |
| | | RPCC/ RAP Subbase | CBR | 67.0 | 70.6 | 330.8 | 18.2 | 27 | 20 | -0.37 |
| | | Subgrade | CBR | 12.9 | 12.1 | 15.6 | 3.9 | 31 | 20 | 1.25 |

Note: DCPI unit is mm/blow; $E_{FWD-K3}$ unit is MPa; CBR unit is %.

**Table 9. Univariate statistics summary of $\gamma_d$ (kN/m$^3$)**

| Field site | TS | Layer | Univariate Statistics | | | | | | |
|---|---|---|---|---|---|---|---|---|---|
| | | | Mean ($\mu$) | Median | Variance ($s^2$) | Std Dev ($\sigma$) | COV | N | Skewness |
| MI I-94 | TS1a | Base | 20.08 | 20.07 | 0.43 | 0.66 | 3 | 54 | -0.37 |
| | TS1b | Base | 20.00 | 20.00 | 0.38 | 0.61 | 3 | 121 | -0.13 |
| | TS3 | Base | 19.21 | 19.25 | 0.77 | 0.88 | 5 | 162 | -0.02 |
| MI I-96 | TS1 | Sand subbase | 20.16 | 20.15 | 0.34 | 0.59 | 3 | 73 | -0.03 |
| | TS2 | CTB | 14.56 | 14.59 | 0.66 | 0.81 | 6 | 119 | -0.3 |
| | TS3 | Sand subbase | 20.01 | 19.89 | 0.26 | 0.51 | 3 | 26 | 0.30 |
| WI US-10 | TS1 | Sandy Subbase | 16.15 | 16.07 | 0.12 | 0.35 | 2 | 17 | -0.3 |
| | TS2 | Subgrade | 19.84 | 19.84 | 0.15 | 0.38 | 2 | 79 | 0.1 |

**Table 10. Univariate statistics summary of *w* (%)**

| Field site | TS | Layer | Univariate Statistics | | | | | | |
|---|---|---|---|---|---|---|---|---|---|
| | | | Mean ($\mu$) | Median | Variance ($s^2$) | Std Dev ($\sigma$) | COV | N | Skewness |
| MI I-94 | TS1a | Base | 1.8 | 1.8 | 0.1 | 0.4 | 22 | 54 | 0.42 |
| | TS1b | Base | 2.3 | 2.3 | 0.1 | 0.3 | 14 | 121 | -0.70 |
| | TS3 | Base | 1.3 | 1.3 | 0.1 | 0.3 | 25 | 162 | 0.44 |
| MI I-96 | TS1 | Sand subbase | 7.8 | 7.7 | 1.0 | 1.0 | 13 | 73 | 0.47 |
| | TS2 | CTB | 7.3 | 7.2 | 1.0 | 1.0 | 14 | 119.0 | 1.4 |
| | TS3 | Sand subbase | 6.3 | 6.3 | 0.5 | 0.7 | 11 | 26 | 0.44 |
| WI US10 | TS1 | Sandy Subbase | 3.7 | 3.7 | 0.2 | 0.5 | 13 | 17.0 | -0.9 |
| | TS2 | Subgrade | 7.5 | 7.4 | 0.9 | 1.0 | 13 | 79.0 | 1.0 |

## Spatial Analysis Results

*Anisotropy in Foundation Layer Properties*

Detailed spatial analysis to assess anisotropy in the measured properties was conducted using the dense grid data set data obtained from two test sections (MI I94 TS1b, and MI I96 TS1). Both omnidirectional and directional semivariograms were studied to assess the anisotropy of each variable over the studied test sections and to examine the need of modeling the possible anisotropy.

The experimental semivariogram of each property variable was calculated as omnidirectional, which assumes an isotropic spatial correlation. Three theoretical semivariogram models, spherical, exponential, and Matérn ($k$=1), are used to fit the experimental semivariogram using weighted least square methods. The model parameters are estimated and the statistical criteria of choosing the better fitted model that including SSErr, GoF, and MSPE are summarized in Table 11.

The estimated model parameters in Table 11 show that there is no single best model type that can better fit the experimental semivariogram than the other two models. The exponential $\hat{\gamma}(h)$ model estimates the largest range or effective range value, a, in most of the cases while the Matérn ($k$=1) model estimates the largest nugget effect, $C_0$, in all cases. The better fitted model is chosen according the statistical criteria to present the results in characterizing and quantifying the isotropic or omnidirectional spatial variability. The smaller value of each of three statistical criteria SSErr, GoF, and MSPE is desired and indicate a better fitted model.

**Table 11. Summary of spatial analysis with omnidirectional semivariogram**

| Project Site | | MI I-94 TS1b | | | MI I-96 TS1 | | |
|---|---|---|---|---|---|---|---|
| | $\hat{\gamma}(\mathbf{h})$ estimation parameters | Model Type | | | Model Type | | |
| Properties | | Sph | Exp | Mat, $k$=1 | Sph | Exp | Mat, $k$=1 |
| $E_{LWD\text{-}Z3}$ (MPa) | $C_0$ | 11.5 | 4.1 | 12.5 | 0 | 0 | 12.2 |
| | Cs | 41.5 | 54.6 | 44.0 | 146.6 | 212.2 | 161.4 |
| | $r$ | 3.2 | 1.5 | 0.9 | 3.4 | 2.7 | 1.2 |
| | a or a' | 3.2 | 4.4 | 3.8 | 3.4 | 8.3 | 5.0 |
| | **SSErr** | 15829 | 15555 | 16009 | 159196 | 170814 | 164420 |
| | **GoF** | 0.0050 | 0.0055 | 0.0054 | 0.0412 | 0.0442 | 0.0417 |
| | **MSPE** | 22.84 | 22.77 | 23.08 | 46.25 | 44.74 | 43.72 |
| $\gamma_d$ (kN/m³) | $C_0$ | 0.15 | 0.13 | 0.16 | 0.05901 | 0.03935 | 0.08359 |
| | Cs | 0.21 | 0.28 | 0.23 | 0.34 | 0.34 | 0.34 |
| | $r$ | 3.4 | 1.9 | 1.1 | 6.9 | 2.966 | 2.238 |
| | a or a' | 3.4 | 5.7 | 4.5 | 6.9 | 8.898 | 8.952 |
| | **SSErr** | 0.1845 | 0.1702 | 0.1723 | 0.1156 | 0.189 | 0.1293 |
| | **GoF** | 0.0024 | 0.0022 | 0.0022 | 0.0104 | 0.0170 | 0.0117 |
| | **MSPE** | 0.2106 | 0.2107 | 0.2115 | 0.135 | 0.1372 | 0.1362 |
| $w$ (%) | $C_0$ | 0.070 | 0.046 | 0.072 | 0.073 | 0.011 | 0.177 |
| | Cs | 0.275 | 0.982 | 0.358 | 1.007 | 1.480 | 1.151 |
| | $r$ | 48.5 | 128.3 | 12.3 | 3.7 | 2.69 | 1.48 |
| | a or a' | 48.5 | 384.9 | 49.4 | 3.7 | 8.07 | 5.94 |
| | **SSErr** | 0.02271 | 0.9678 | 0.01504 | 5.168 | 5.39 | 5.277 |
| | **GoF** | 0.0031 | 0.0784 | 0.0021 | 0.0399 | 0.0427 | 0.0421 |
| | **MSPE** | 0.0807 | 0.08093 | 0.0811 | 0.3937 | 0.4124 | 0.4085 |
| $DCPI_{subbase}$ (mm/blow) | $C_0$ | 0.53 | 0.30 | 0.51 | 0 | 0 | 0 |
| | Cs | 0.70 | 0.97 | 0.76 | 26.57 | 46.05 | 30.95 |
| | $r$ | 2.20 | 0.82 | 0.60 | 3.80 | 3.92 | 1.23 |
| | a or a' | 2.20 | 2.45 | 2.41 | 3.80 | 11.77 | 4.93 |
| | **SSErr** | 5.364 | 5.565 | 5.31 | 2387 | 2608 | 2302 |
| | **GoF** | 0.0027 | 0.0025 | 0.0024 | 0.0728 | 0.0737 | 0.0702 |
| | **MSPE** | 0.9048 | 0.8679 | 0.8701 | 11.76 | 11.97 | 11.95 |
| $DCPI_{subgrade}$ (mm/blow) | $C_0$ | 0 | 0 | 0 | 2.1 | 0 | 0 |
| | Cs | 57.6 | 58.8 | 58.6 | 4.0 | 6.0 | 5.6 |
| | $r$ | 0.85 | 0.30 | 0.21 | 4.1 | 1.1 | 0.6 |
| | a or a' | 0.85 | 0.91 | 0.84 | 4.1 | 3.3 | 2.4 |
| | **SSErr** | 16893 | 21970 | 19925 | 179.5 | 170.2 | 169.4 |
| | **GoF** | 0.0022 | 0.0022 | 0.0021 | 0.0390 | 0.0424 | 0.0461 |
| | **MSPE** | 60.3 | 60.41 | 60.48 | 3.455 | 3.514 | 3.56 |

### MI I94 TS1b

The omnidirectional experimental semivariograms and the kriged contour maps separately for all parameters obtained from the MI I-94 TS1b are shown in in Figure 16 to Figure 25. The kriged contours were generated using the model selected based on the smallest MSPE. Some key observations assessing the semivariograms and the contour plots are as follows:

- The sill of the omnidirectional γ(h) of $E_{LWD\text{-}Z3}$ is higher than the sample variance slightly which indicates a possible trend in the data or an anisotropic semivariogram (Figure 16). The

contour plot for $E_{LWD-Z3}$ shows that there is less variability in the data in transverse direction than in the longitudinal direction (Figure 17). Based on these observations, further analysis with directional variability should be performed on this dataset to identify correlation length in different directions.

- Omnidirectional $\gamma(h)$ of $\gamma_d$ showed increasing $\gamma(h)$ with separation distance and close to the sample variance (Figure 18), and the nugget values of $\hat{\gamma}(h)$ are relatively larger compared to its sill value. The measurement error or insufficient sampling at smaller spacing might be the cause for the relatively high nugget value. The contour plot (Figure 19) shows that the upper left portion of the studied area had comparatively low values and the bottom left portion had comparatively high areas.

- Omnidirectional $\gamma(h)$ of moisture content shows a very large nugget effect compared to the sample variance and a trend can be observed in the fitted semivariogram with range estimated as about 50 m (Figure 20). The experimental omnidirectional $\gamma(h)$ calculated in this study area is close to a straight line and there appears to be a trend in the data with moisture content decreasing from the top left corner to the bottom right corner (Figure 21).

- The omnidirectional $\gamma(h)$ of $DCPI_{subbase}$ and $DCPI_{subgrade}$ are shown in Figure 22 and Figure 24, respectively. A longer range value was observed in $DCPI_{subbase}$ than $DCPI_{subgrade}$ which indicates that there is a higher spatial correlation in $DCPI_{subbase}$ values than $DCPI_{subgrade}$ values. The experimental semivariogram calculated for $DCPI_{subbase}$ shows a nearly zero nugget effect, only a few $\gamma(h)$ values within the first 1 m separation distance show a possible correlation of $DCPI_{subgrade}$ with spacing distance. The zero nugget effect and short range value modeled in $DCPI_{subgrade}$ predicted values at unsampled location around the sampled location with variation equal to the sill value which shows up as concentrated small circular areas with similar values in the kriged contour plot of $DCPI_{subgrade}$ (Figure 25). The $DCPI_{subbase}$ contour plot shows less concentrated circular areas than $DCPI_{subgrade}$, which is indicative of the longer range values.
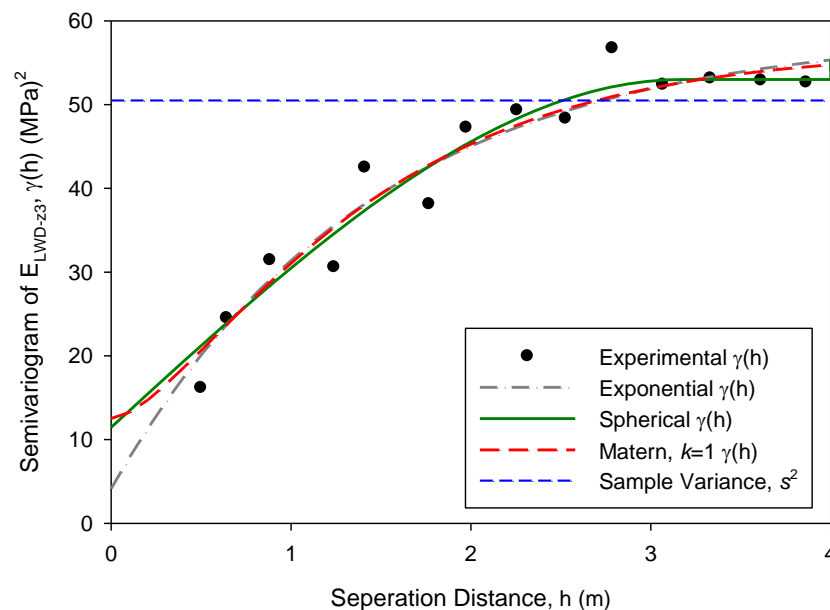


**Figure 16. MI I94 TS1b: Omnidirectional $\gamma(h)$ of $E_{LWD-Z3}$ with fitted $\hat{\gamma}(h)$**
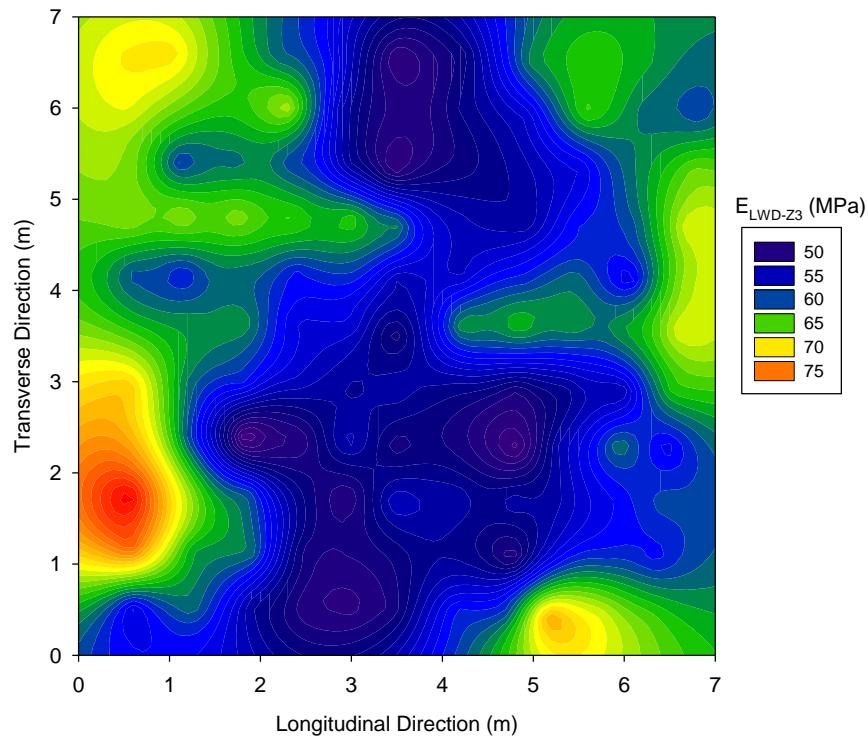
28

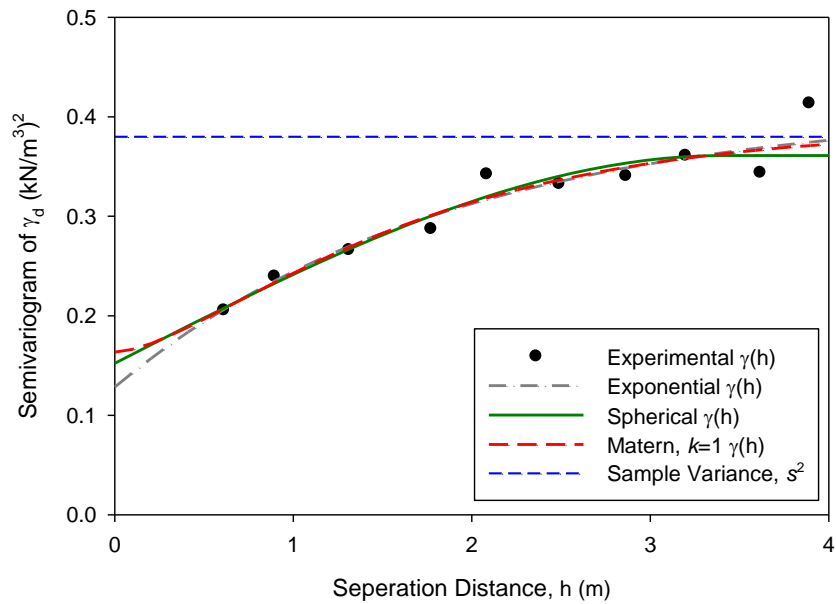**Figure 17. MI I94 TS1b: Ordinary kriging of $E_{LWD-Z3}$ with fitted omnidirectional exponential $\hat{\gamma}(\mathbf{h})$**



**Figure 18. MI I94 TS1b: Omnidirectional $\gamma(\mathbf{h})$ of $\gamma_d$ with fitted $\hat{\gamma}(\mathbf{h})$**
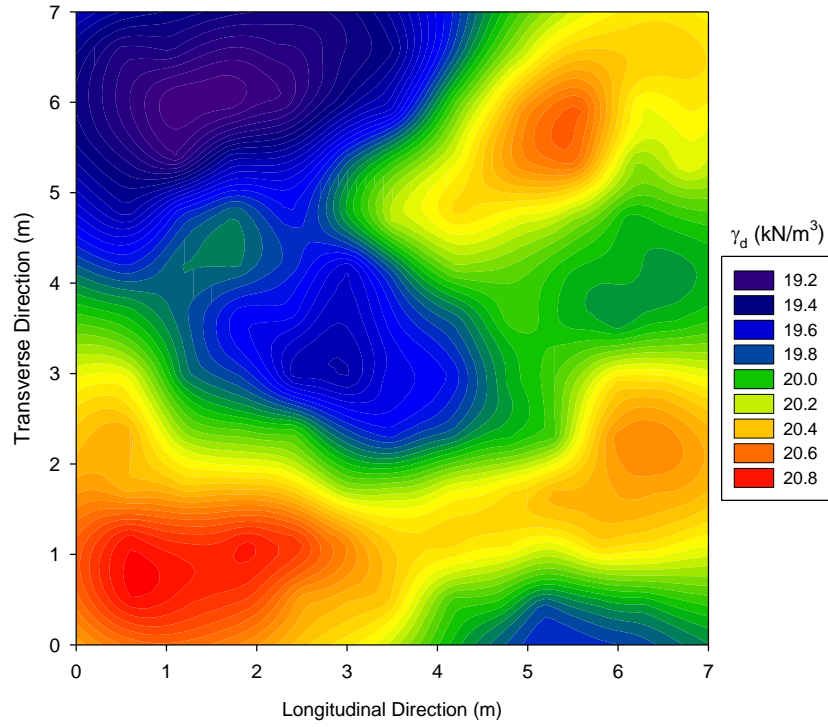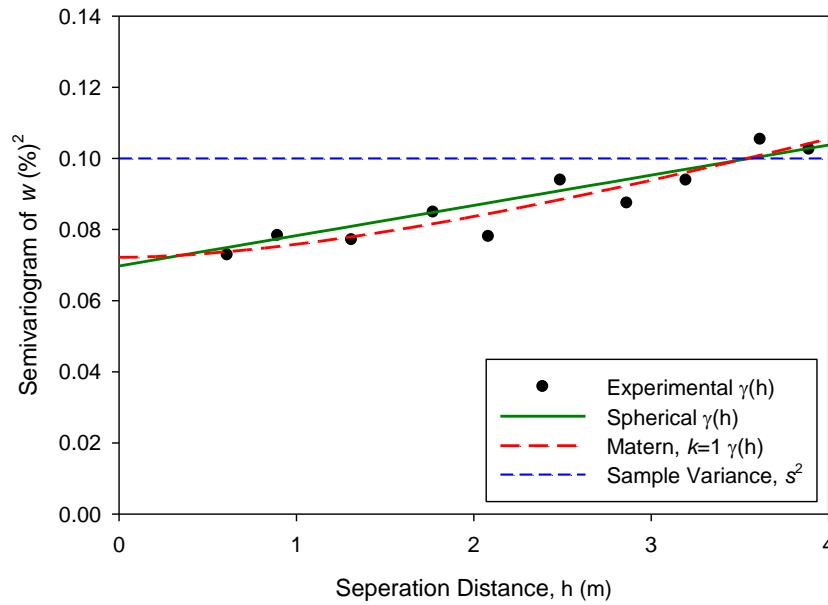
**Figure 19. MI I94 TS1b: Ordinary kriging of $\gamma_d$ with fitted omnidirectional spherical $\hat{\gamma}(h)$**



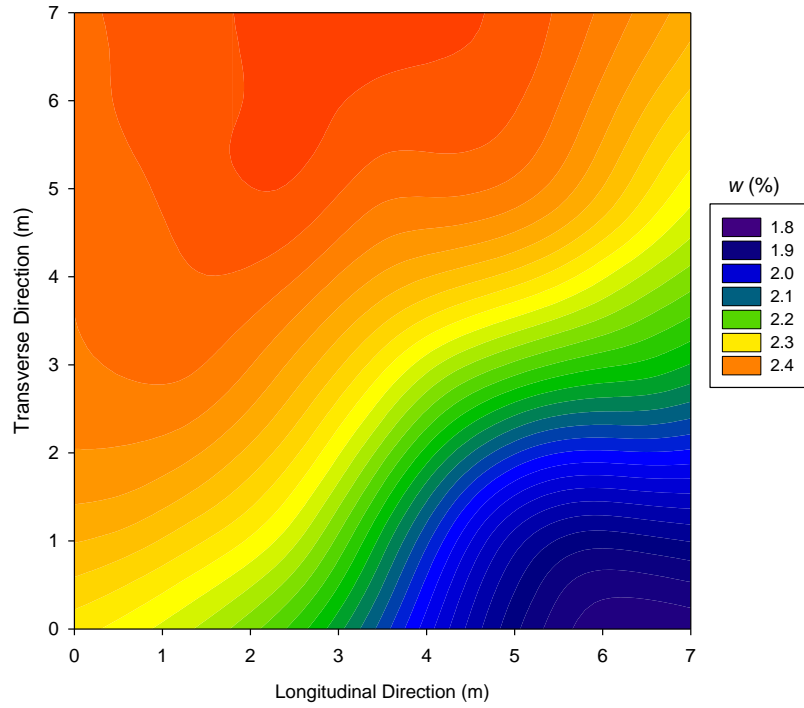**Figure 20. MI I94 TS1b: Omnidirectional $\gamma(h)$ of $w$ with fitted $\hat{\gamma}(h)$**

**Figure 21. MI I94 TS1b: Ordinary kriging of *w* with fitted omnidirectional exponential $\hat{\gamma}(\mathbf{h})$**
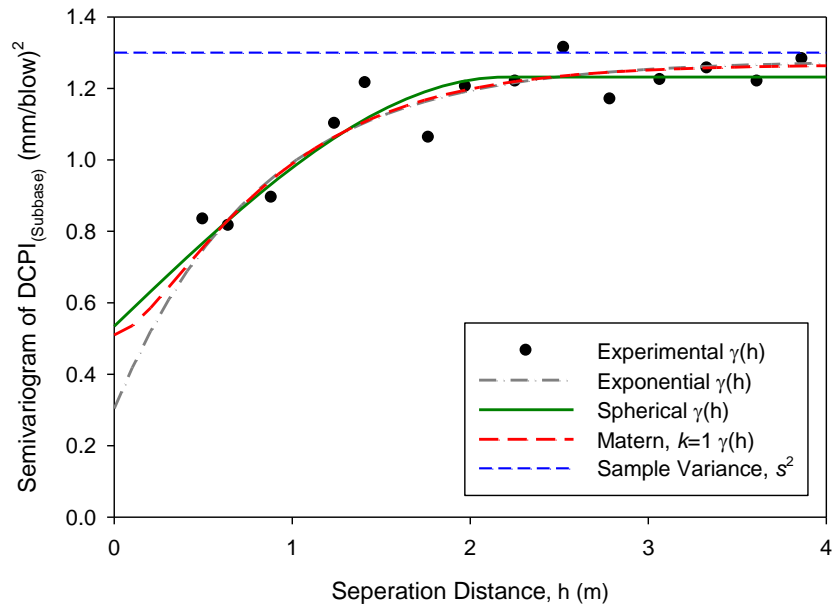


**Figure 22. MI I94 TS1b: Omnidirectional γ(h) of DCPI_subbase with fitted $\hat{\gamma}(\mathbf{h})$**
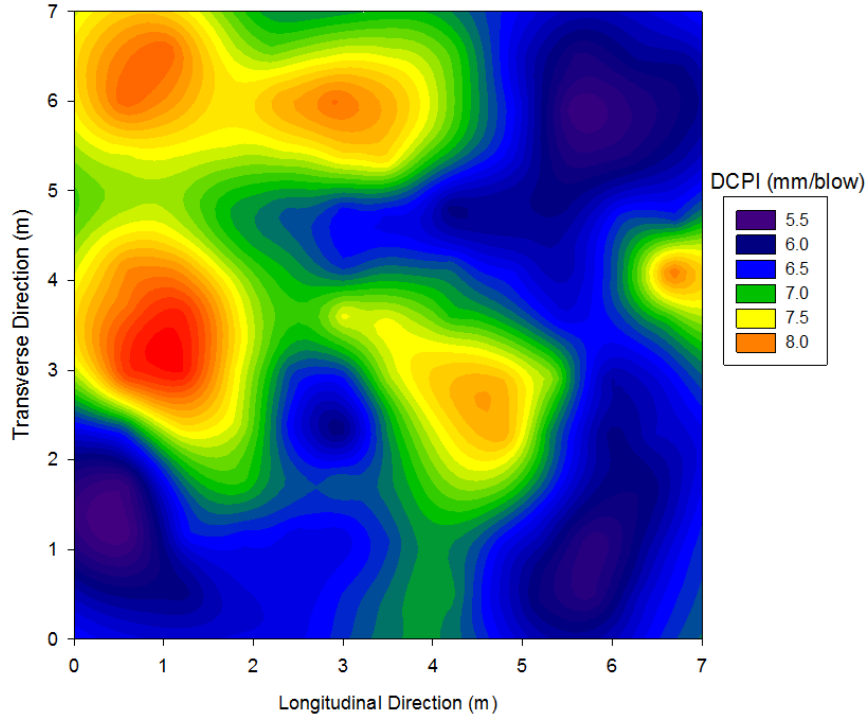
**Figure 23. MI I94 TS1b: Ordinary kriging of DCPI$_{subbase}$ with fitted omnidirectional spherical $\hat{\gamma}(h)$**
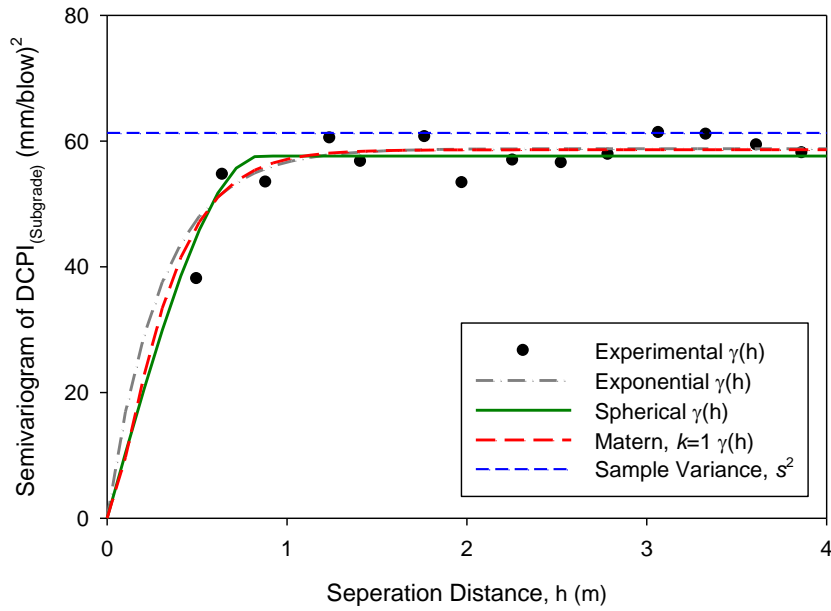


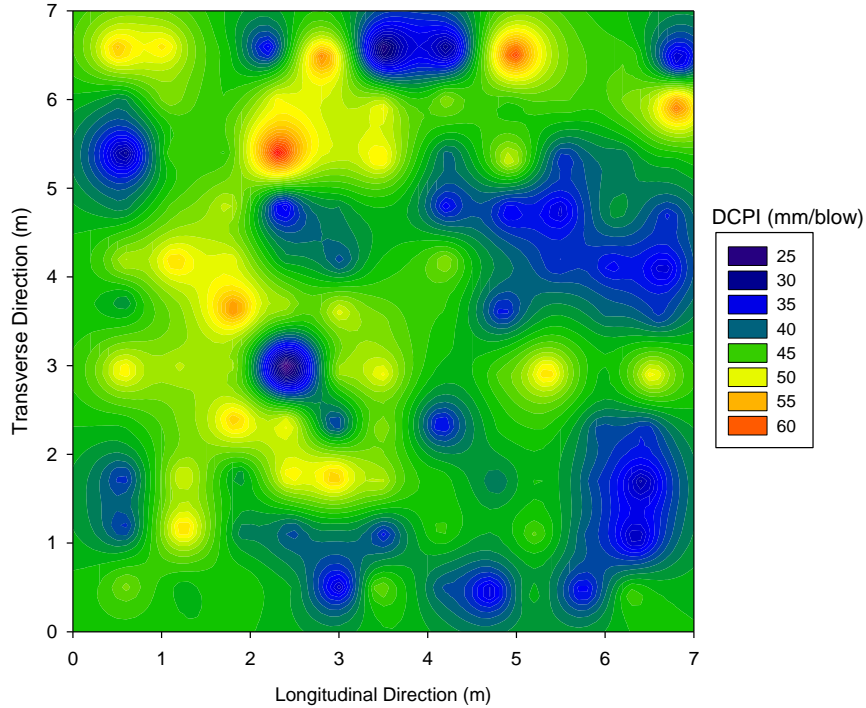**Figure 24. MI I94 TS1b: Omnidirectional $\gamma(h)$ of DCPI$_{subgrade}$ with fitted $\hat{\gamma}(h)$**

**Figure 25. MI I94 TS1b: Ordinary kriging of DCPI$_{subgrade}$ with fitted omnidirectional spherical $\hat{\gamma}(\mathbf{h})$**

MI I96 TS1

The omnidirectional experimental semivariograms and the kriged contour maps separately for all parameters obtained from the MI I96 TS1 are shown in Figure 26 to Figure 35. Some key observations assessing the semivariograms and the contour plots are as follows:

- Omnidirectional $\gamma(h)$ of $E_{LWD-Z3}$ increased with separation distance and exceeds the sample variance before the fitted model predicted range is reached (Figure 26). This indicates a possible trend or anisotropy behavior in the data, which is also confirmed in the contour plot (Figure 27). Anisotropy of the directional semivariogram should be investigated for this data set.
- Omnidirectional $\gamma(h)$ of $\gamma_d$ measurements shows a possible trend with long spatial correlation. The range value, estimated as about 6.9 m with spherical model and is larger than the maximum semivariogram study distance of 4 m (Figure 28). The contour plot (Figure 29) of $\gamma_d$ shows two sections with higher values at the upper portion of the plot and lower valuea at the lower portion. This indicates that anisotropy should be investigated for the collected $\gamma_d$ values.
- Omnidirectional $\gamma(h)$ of *w* measurements shows a possible trend because $\gamma(h)$ is larger than the sample variance after about 3 m separation distance (Figure 30). The contour plot (Figure 31) also shows higher values in the bottom half than in the top half. Investigating anisotropy is advised for the collected *w* values.

- Omnidirectional $\gamma(h)$ of $DCPI_{subbase}$ also shows a possible trend with $\gamma(h)$ larger than the sample variance after about 2 m separation distance (Figure 32). The $DCPI_{subbase}$ contour plot (Figure 33) shows somewhat similar trends as the $E_{LWD-Z3}$ contour plot.
- Omnidirectional $\gamma(h)$ of $DCPI_{subgrade}$ did not show clear spatial correlation with separation distance.



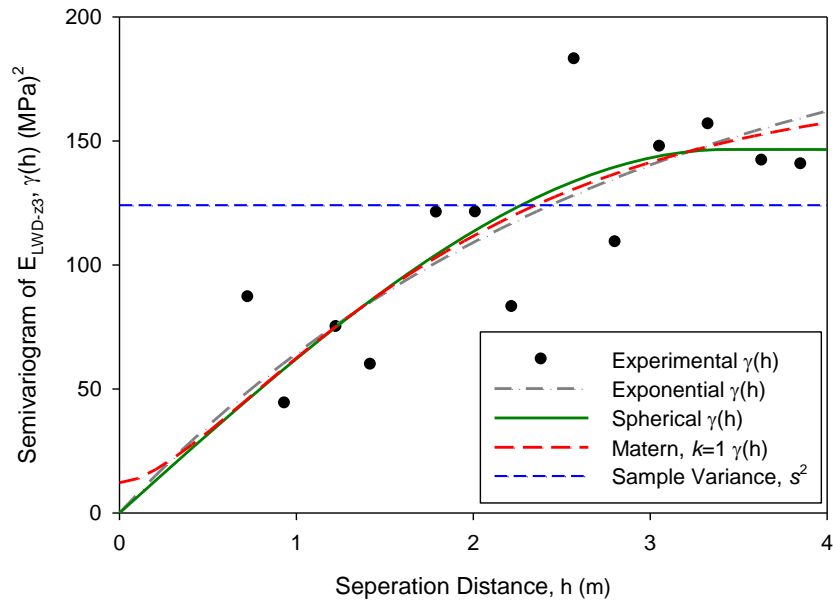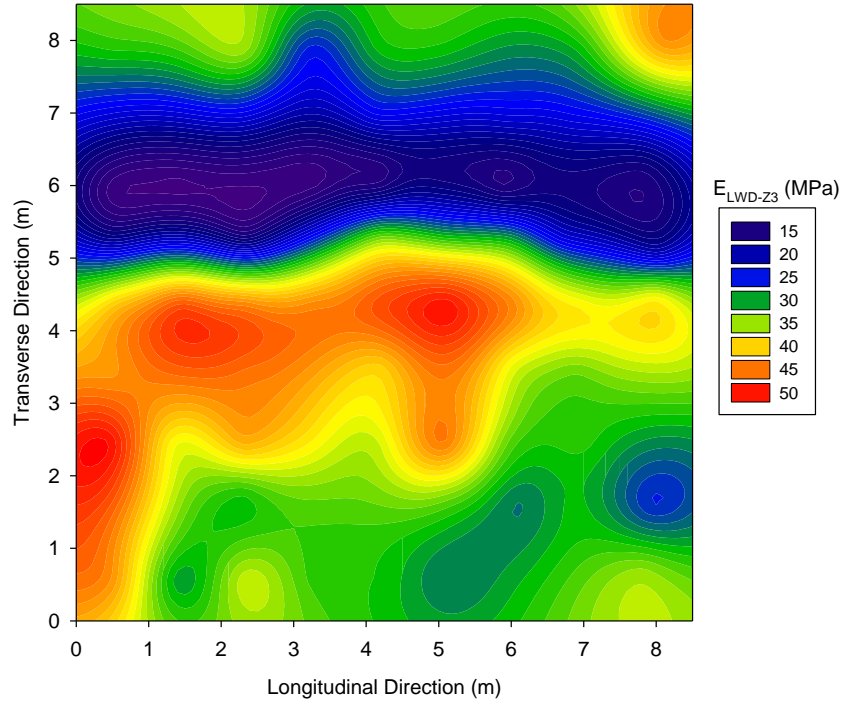**Figure 26. MI I96 TS1: Omnidirectional $\gamma(h)$ of $E_{LWD-Z3}$**

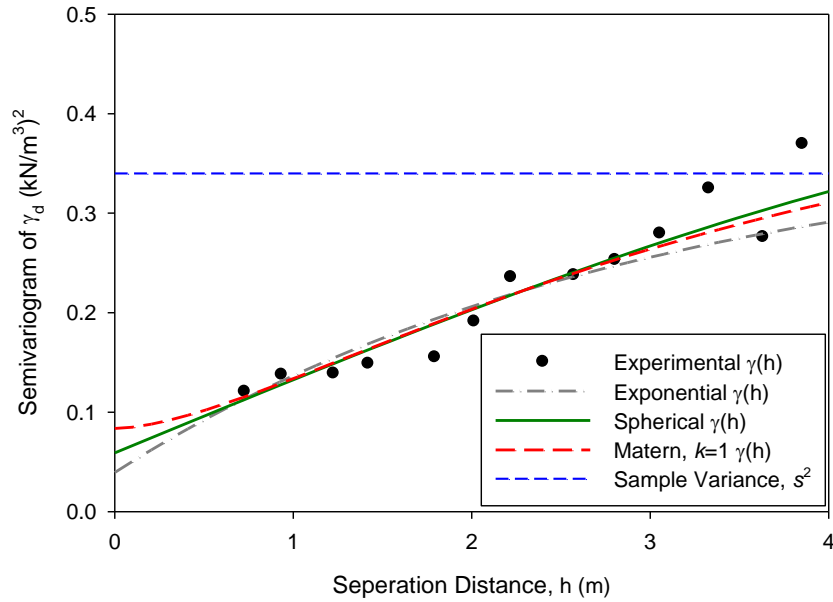**Figure 27. MI I96 TS1: Ordinary kriging of $E_{LWD\text{-}Z3}$ with fitted omnidirectional Matérn (k=1) $\hat{\gamma}(\mathbf{h})$**



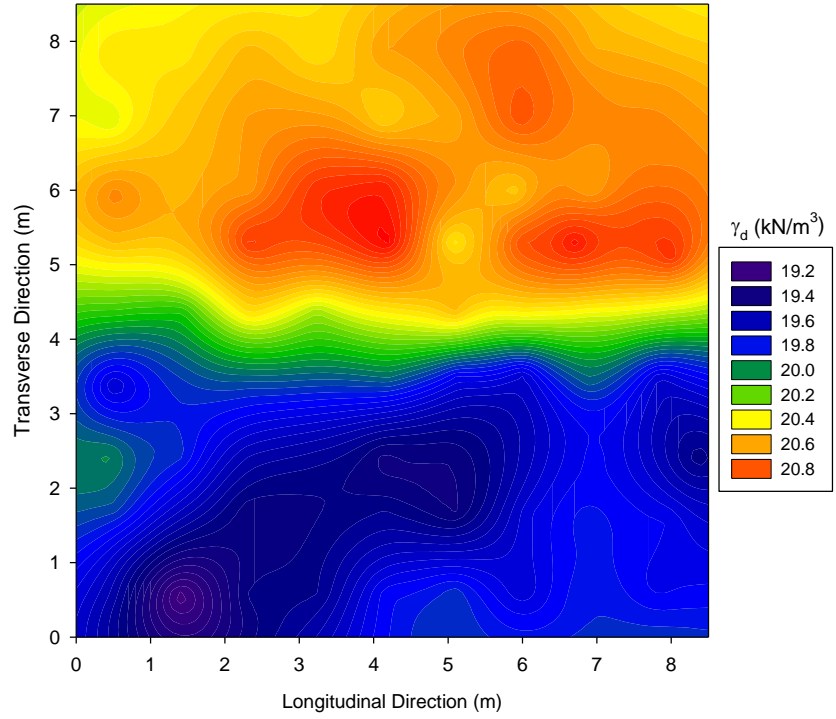**Figure 28. MI I96 TS1: Omnidirectional $\gamma(\mathbf{h})$ of $\gamma_d$ with fitted $\hat{\gamma}(\mathbf{h})$**

35

**Figure 29. MI I96 TS1: Ordinary kriging of γ(h) with fitted omnidirectional spherical γ̂(h)**



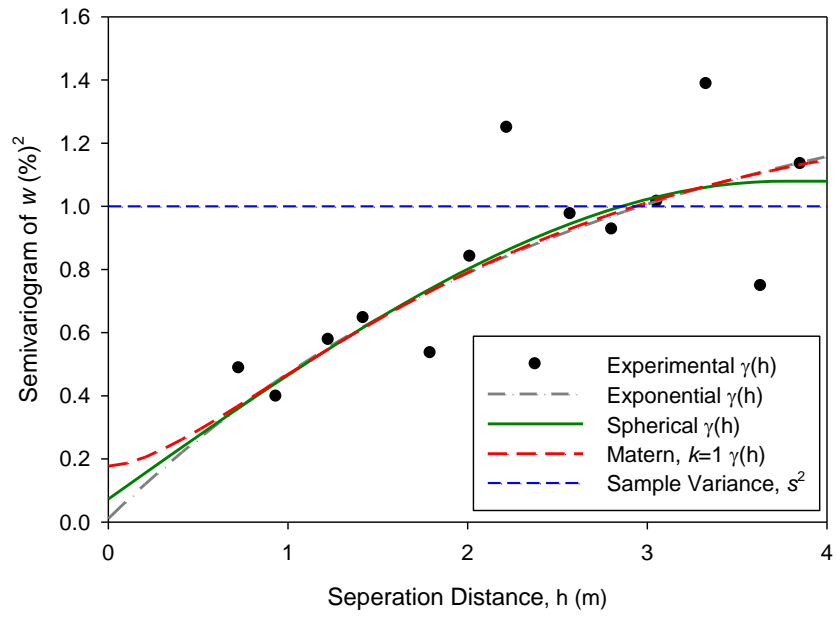**Figure 30. MI I96 TS1: Omnidirectional γ(h) of *w* with fitted γ̂(h)**

**Figure 31. MI I96 TS1: Ordinary kriging of *w* with fitted omnidirectional spherical $\hat{\gamma}(\mathbf{h})$**



**Figure 32. MI I96 TS1: Omnidirectional γ(h) of DCPI_subbase with fitted $\hat{\gamma}(\mathbf{h})$**
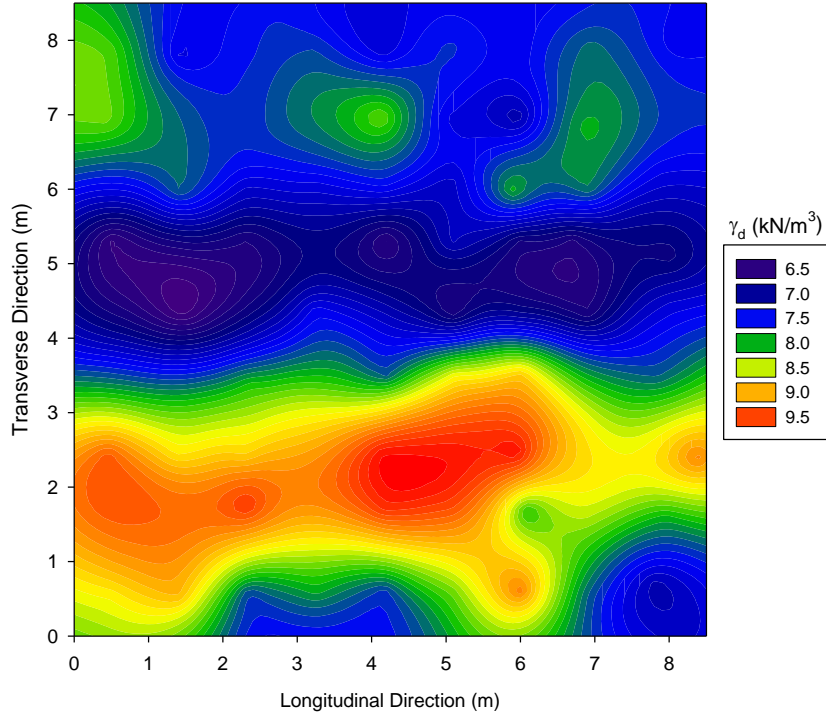
**Figure 33. MI I96 TS1: Ordinary kriging of DCPI_subbase with fitted omnidirectional spherical $\hat{\gamma}(h)$**
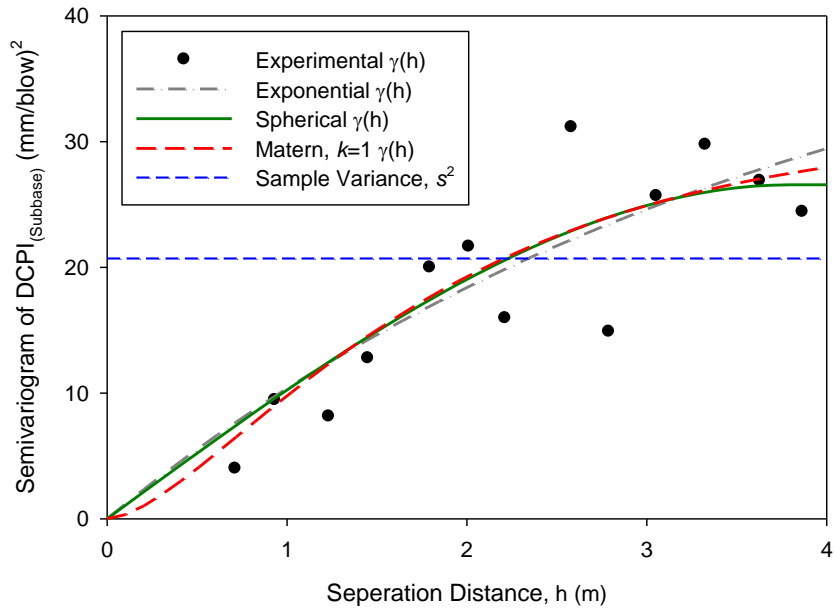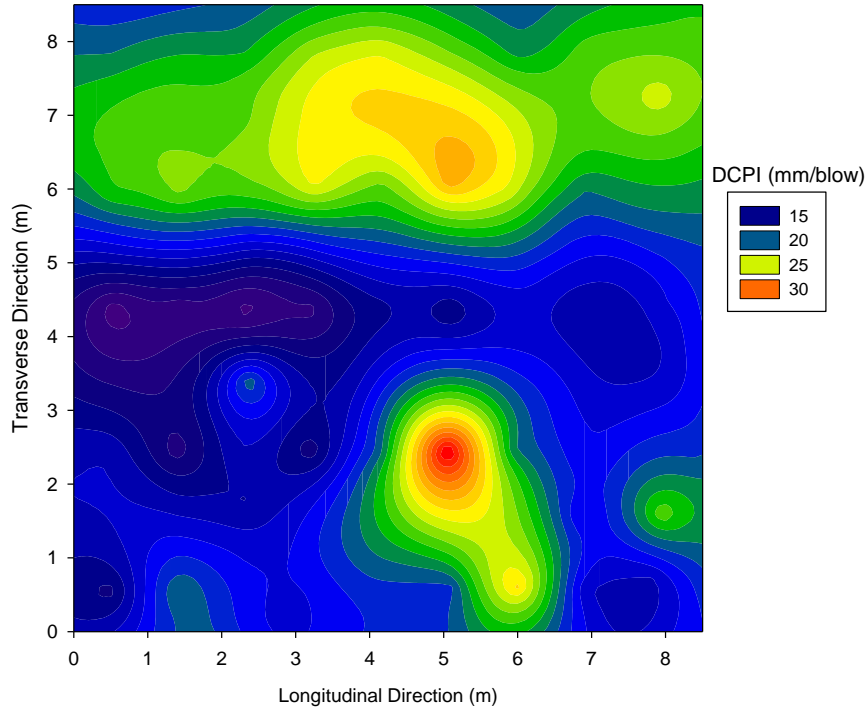


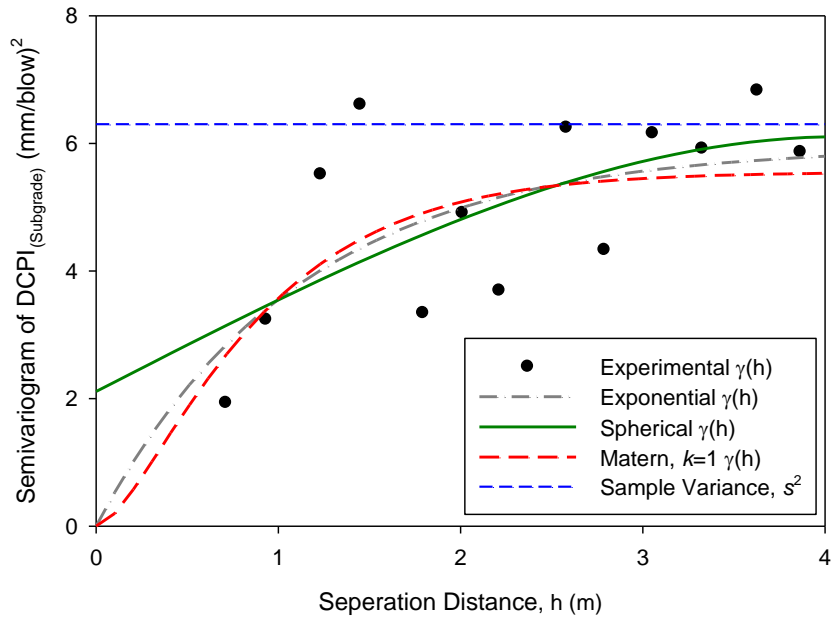**Figure 34. MI I96 TS1: Omnidirectional $\gamma(h)$ of DCPI_subgrade with fitted $\hat{\gamma}(h)$**
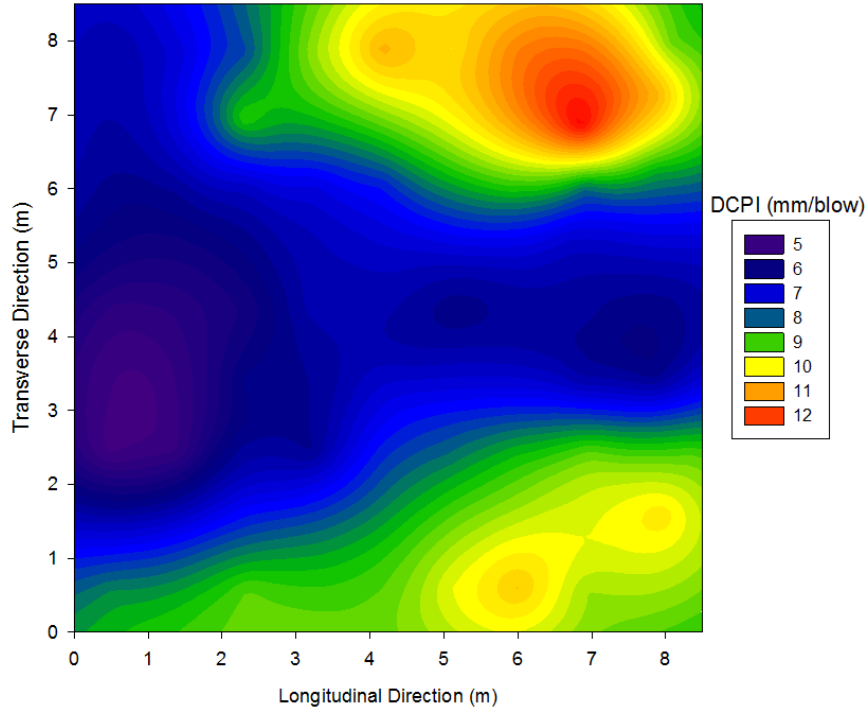
**Figure 35. MI I96 TS1: Ordinary kriging of DCPI_subgrade with fitted omnidirectional spherical $\hat{\gamma}(h)$**

*Directional Semivariogram Anisotropy Modeling*

Directional experimental semivariograms are studied to identify anisotropic behavior of the measuredvariables. A rose diagram, semivariogram map, semivariogram contour map, and directional semivariograms helps identifying anisotropic behavior. As noted above, the kriged contour plots with omnidirectional experimental semivariogram of some of the pavement foundation properties revealed the need for directional semivariograms. The anisotropic $\gamma(h)$ is modeled by fitting the theoretical semivariogram model with the identified anisotropy ratio ($\lambda$), major direction ($\delta$) for both geometric and zonal anisotropy, and a nested model for zonal anisotropy. Directional $\gamma(h)$ is calculated in four major directions ($\theta = 0°, 45°, 90°, 135°$) and the major and minor directions are generally at $\theta$ equals to $0°$ and $90°$ which aligns with transverse and longitudinal directions of pavement sections. All three theoretical models (i.e., spherical, exponential, and Matérn with k=1) are fitted to the $\gamma(h)$ in major and minor directions individually, and the best fitted model of the three are selected based on the smallest SSErr value and summarized in Table 12. For illustration purposes, the process for constructing directional semivariograms is shown for $E_{LWD-Z3}$ measurements obtained from MI I94 TS1b. Four types of plots, directional semivariograms, a rose diagram, a semivariogram map, and a semivariogram contour map for preliminary examination of the directional variation of sill and range parameters. The process is summarized as follows:

- First, the range values are determined and recorded for each directional $\gamma(h)$ plot (Figure 36).

- Second, a rose diagram of range values is created by identifying the range values at each directional $\gamma$(h) with a selected $\gamma$(h) that is not the initial value nor the constant $\gamma$(h) in all directions, as shown in Figure 37. An ellipse that indicates geometric anisotropy is closely fitted to the end points of range values along the axial directions (Figure 37).
- Third, a semivariogram map is created by setting a lag distance and calculating the average value of all $\gamma(\boldsymbol{h})$ falling into the area cell with the side distance the same as the lag distance. The lag distance should be chosen as a value not smaller than the minimum spacing that point pairs are apart. Figure 38 is the semivariogram map using a color scheme to represent the value of the average $\gamma$(h) in each area cell and Figure 39 is the semivariogram contour map that plots the same values in a contour line. Both these plots show zonal anisotropy with $E_{LWD-Z3}$ being less variable in transverse direction compared to the longitudinal direction.
- The semivariogram models fitted in transverse (y) direction and longitudinal (x) direction are shown in Figure 40. The fitted $\hat{\gamma}$(h) in the longitudinal direction exceeded the sample variance while the fitted $\hat{\gamma}$(h) in transverse direction reached a constant value that is below the sample variance at a small range value. However, the experimental semivariogram $\gamma$(h) tends to increase at separation distances over 3 m.
- With the fitted $\hat{\gamma}$(h) in both transverse and longitudinal directions, the best fitted model could be selected with the smaller SSErr and GoF values. The first isotropic part of zonal anisotropy is modeled with the selected model for the transverse direction $\hat{\gamma}_1$(h) that has the lower sill than the longitudinal direction. Then the second part of zonal anisotropy $\hat{\gamma}_2(\boldsymbol{h})$ is modeled with the model selected for the longitudinal direction with range set to be extremely large (e.g., $10^9$) and high zonal anisotropy ratio ($\lambda$) ($\lambda \times 10^9$). Figure 41 shows the nested model with zonal anisotropy fitted $\hat{\gamma}$(h) is shown as a continuous curve in comparison with the experimental semivariogram of $E_{LWD-Z3}$ shown as black dots in different directions. The kriged contour plot using the zonal anisotropic model for $E_{LWD-Z3}$ shown in Figure 35.

**Table 12. Summary of theoretical model fitted to major and minor directional γ(h)**

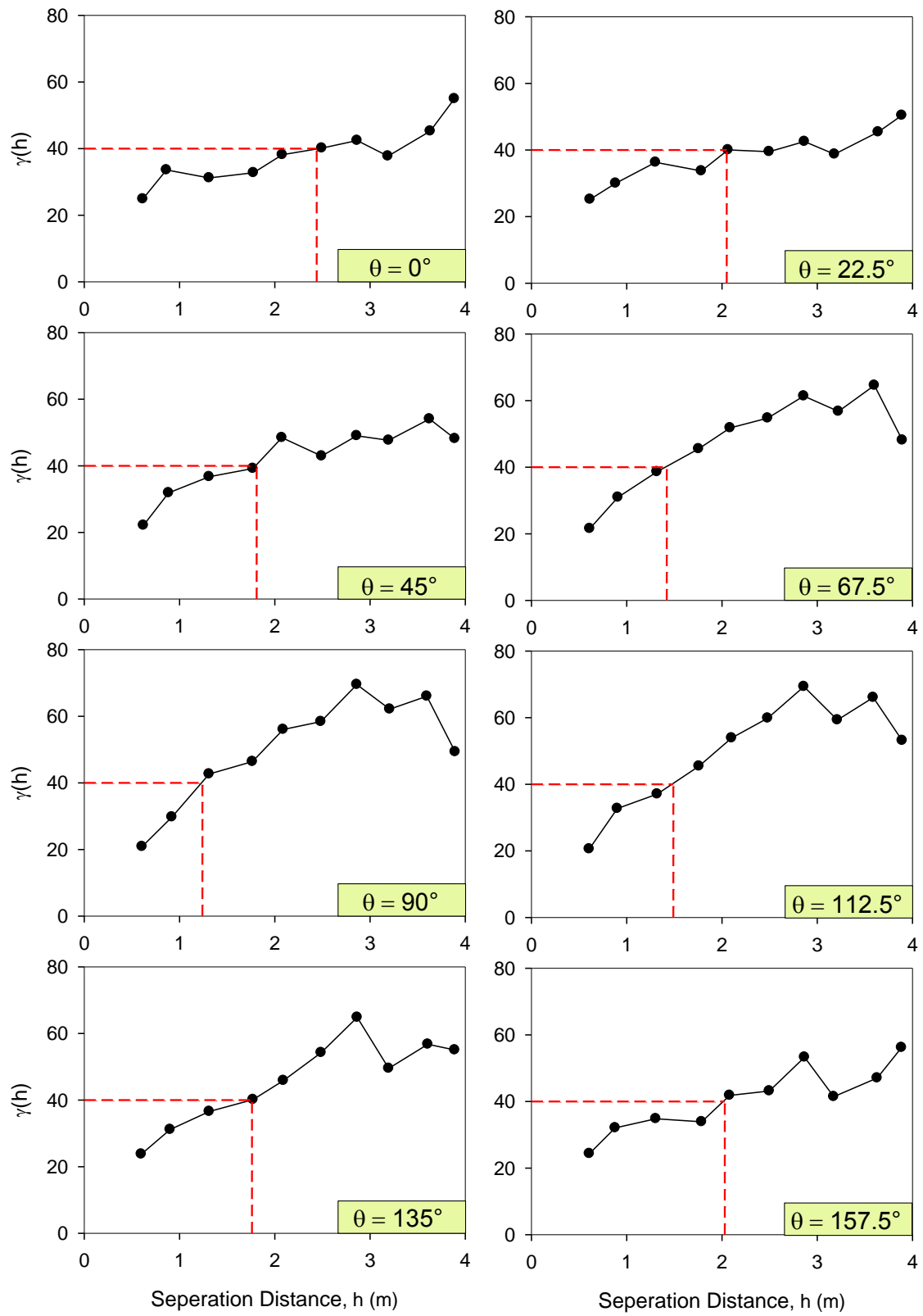| | Project Site | MI I-94 TS1b | | MI I-96 TS1 | |
|---|---|---|---|---|---|
| **Properties** | $\hat{\gamma}(h)$ estimation parameters | **Transverse Direction, y, θ=0°** | **Longitudinal Direction, x, θ=90°** | **Transverse Direction, y, θ=0°** | **Longitudinal Direction, x, θ=90°** |
| $E_{LWD\text{-}z3}$ (MPa) | Model | Exp | Sph | Sph | Mat, k=1 |
| | $C_0$ | 20.3 | 3.229 | 3.931 | 0 |
| | Cs | 38.78 | 59.79 | 161.37 | 203.5 |
| | $r$ | 3.674 | 2.993 | 2.624 | 2.071 |
| | a or a′ | 11.022 | 2.993 | 2.624 | 8.284 |
| | **SSErr** | 6481 | 6112 | 193699 | 151449 |
| | **GoF** | 0.0066 | 0.0087 | 0.0652 | 0.2323 |
| $\gamma_d$ (kN/m³) | Model | Sph | Sph | Sph | Mat, k=1 |
| | $C_0$ | 0.1523 | 0.14 | 0 | 0 |
| | Cs | 0.1965 | 0.4844 | 0.674 | 0.1661 |
| | $r$ | 2.328 | 9.86 | 7.482 | 0.558 |
| | a or a′ | 2.328 | 9.86 | 7.482 | 2.232 |
| | **SSErr** | 0.07408 | 0.4511 | 0.3866 | 0.1554 |
| | **GoF** | 0.0014 | 0.0107 | 0.0375 | 0.1090 |
| $w$ (%) | Model | Sph (θ=45°) | Mat, k=1 (θ=135°) | Sph | Exp |
| | $C_0$ | 0.075137 | 0.06748 | 0 | 0 |
| | Cs | 0.006446 | 512.38299 | 1.406 | 0.8321 |
| | $r$ | 1.971 | 604.6 | 3.531 | 1.785 |
| | a or a′ | 1.971 | 2418.4 | 3.531 | 5.355 |
| | **SSErr** | 0.01376 | 0.01185 | 3.826 | 4.215 |
| | **GoF** | 0.0087 | 0.0024 | 0.0276 | 0.1813 |
| $DCPI_{sub\,base}$ (mm/blow) | Model | Sph | Mat, k=1 | Matern, k=1 | Spherical |
| | $C_0$ | 0.6996 | 0.1071 | 0 | 0.4807 |
| | Cs | 0.4956 | 1.189 | 30.21 | 27.5117 |
| | $r$ | 1.732 | 0.5448 | 1.072 | 4.603 |
| | a or a′ | 1.732 | 2.1792 | 4.288 | 4.603 |
| | **SSErr** | 7.769 | 1.201 | 2705 | 2015 |
| | **GoF** | 0.0094 | 0.0021 | 0.1781 | 0.1367 |
| $DCPI_{sub\,grade}$ (mm/blow) | Model | | | Spherical | Spherical |
| | $C_0$ | | | 0 | 0 |
| | Cs | Direction semivariogram shows pure nugget effect, there no additional modeling performed. | | 5.865 | 4.152 |
| | $r$ | | | 1.068 | 2.289 |
| | a or a′ | | | 1.068 | 2.289 |
| | **SSErr** | | | 469.8 | 283.2 |
| | **GoF** | | | 0.1352 | 0.1760 |

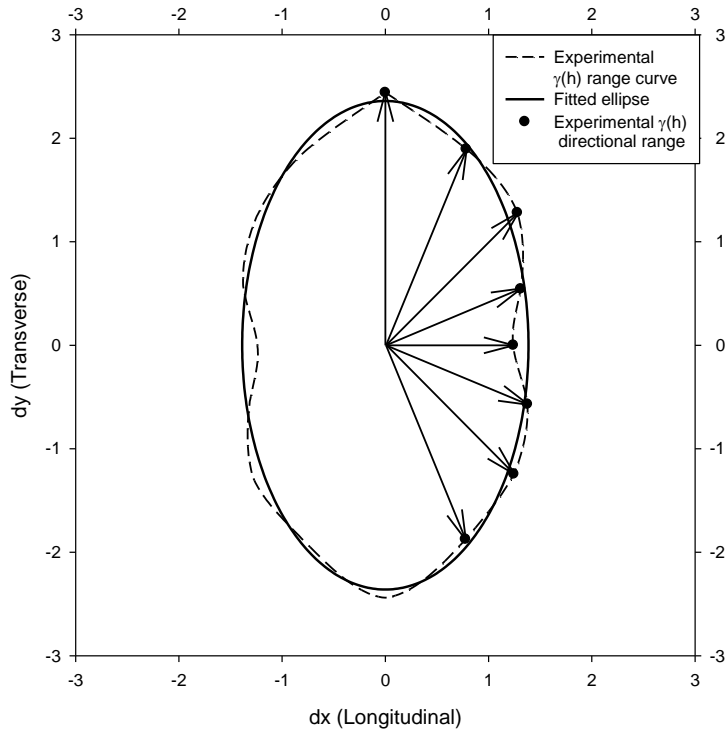**Figure 36. Directional γ(h) of E<sub>LWD-Z3</sub> on MI I94 TS1b**

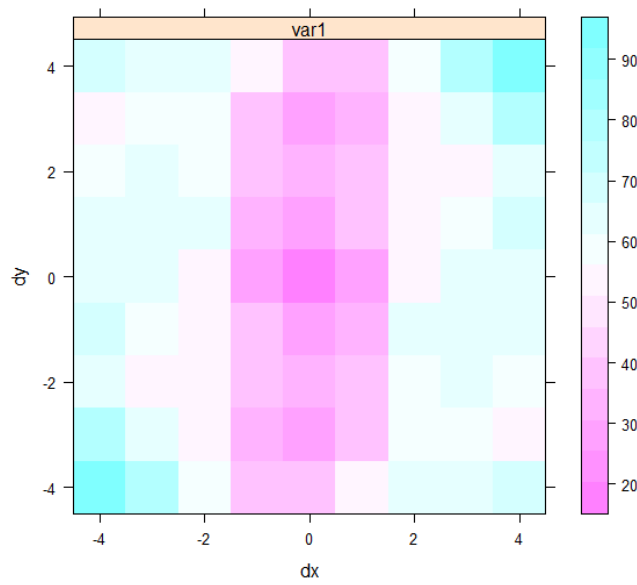**Figure 37. Rose diagram of E$_{LWD-Z3}$ on MI I94 TS1b**



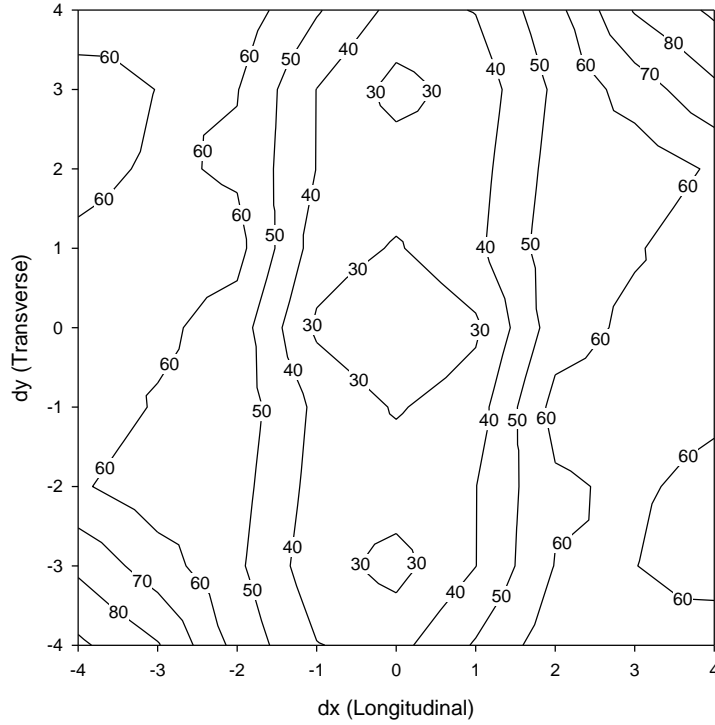**Figure 38. Semivariogram map of E$_{LWD-Z3}$ on MI I94 TS1b**

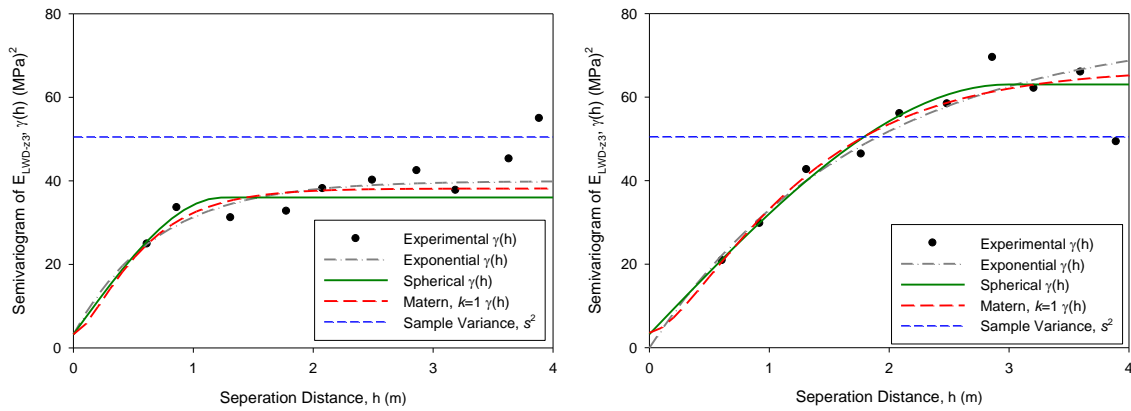**Figure 39. Semivariogram contour map of $E_{LWD-Z3}$ on MI I94 TS1b**



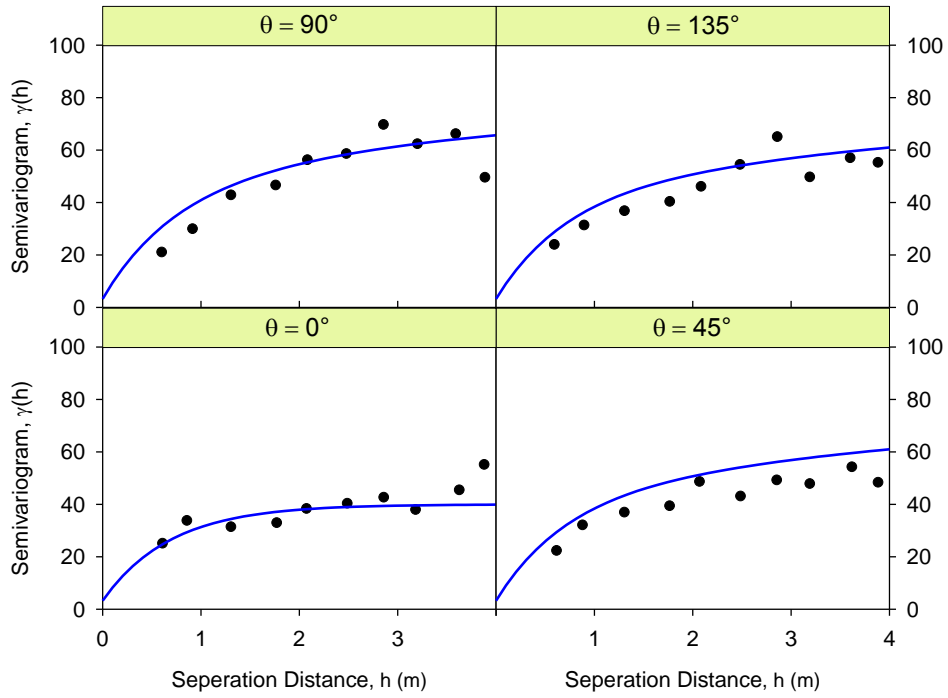**Figure 40. Fitted $\hat{\gamma}(h)$ for $E_{LWD-Z3}$ on MI I94 TS1b, transverse direction (left) and longitudinal (right)**

**Figure 41. Modelling γ(h) with zonal anisotropy for E$_{LWD-Z3}$ on MI I94 TS1b**
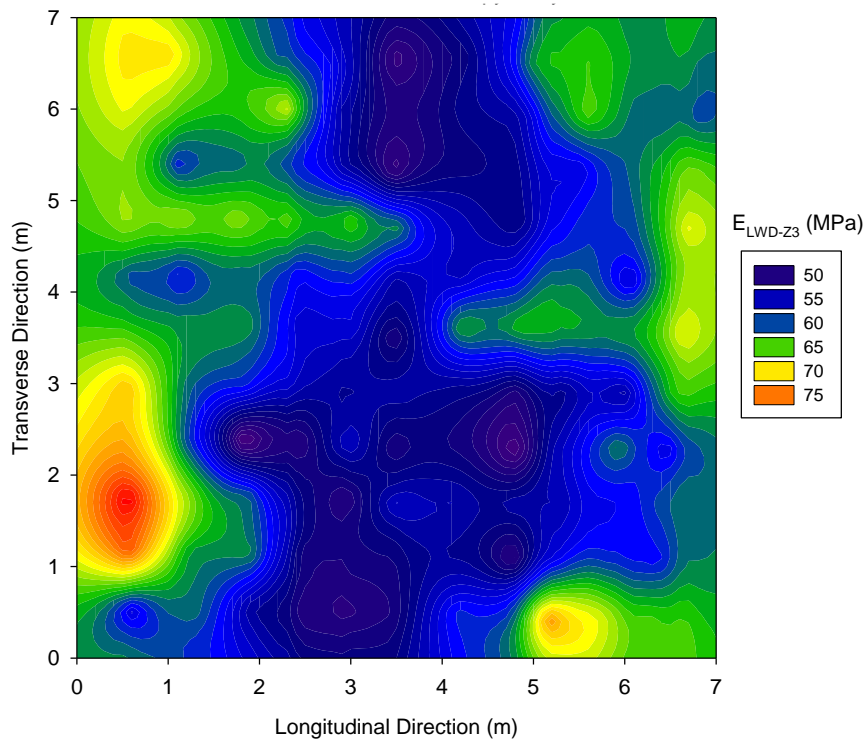


**Figure 42. Kriged contour plot of E$_{LWD-Z3}$ on MI I94 TS1b**

A summary of sill and range values estimated by weighted least squares fitted theoretical semivariogram models for omnidirectional and directional semivariogram analysis are summarized in Table 13.

**Table 13. Summary of omnidirectional and directional variogram parameters**

| In-situ properties | Directions | MI I-94 TS1b | | MI I-96 TS1 | |
|---|---|---|---|---|---|
| | | Sill $(C+C_0)$ | Range (a or a'), m | Sill $(C+C_0)$ | Range (a or a'), m |
| $E_{LWD-Z3}$ (MPa) | Omnidirection | 58.8 | 4.4 | 173.6 | 5.0 |
| | Transverse Direction (y) | 59.1 | 11.0 | 165.3 | 2.6 |
| | Longitudinal Direction (x) | 63.0 | 3.0 | 203.5 | 8.3 |
| $\gamma_d$ (kN/m$^3$) | Omnidirection | 0.36 | 3.4 | 0.40 | 6.9 |
| | Transverse Direction (y) | 0.35 | 2.3 | 0.67 | 7.5 |
| | Longitudinal Direction (x) | 0.62 | 9.9 | 0.17 | 2.2 |
| w (%) | Omnidirection | 0.345 | 48.5 | 1.079 | 3.757 |
| | Transverse Direction (y) | — | | 1.406 | 3.531 |
| | Longitudinal Direction (x) | | | 0.832 | 5.355 |
| $DCPI_{subbase}$ (mm/blow) | Omnidirection | 1.28 | 2.5 | 26.57 | 4.09 |
| | Transverse Direction (y) | 1.20 | 1.7 | 30.21 | 4.30 |
| | Longitudinal Direction (x) | 1.30 | 2.2 | 27.99 | 4.60 |
| $DCPI_{subgrade}$ (mm/blow) | Omnidirection | 57.6 | 0.8 | 6.1 | 3.8 |
| | Transverse Direction (y) | — | | 5.9 | 1.1 |
| | Longitudinal Direction (x) | | | 4.2 | 2.3 |

*Analysis of Sparse versus Dense Grid Sampling for Anisotropy*

In this section, results of dense and sparse datasets obtained from the same project are compared using directional and omnidirectional experimental semivariograms. The results are compared in Table 14. Semivariograms for directional spatial variability are presented for $E_{LWD-Z3}$, $\gamma_d$, and $DCPI_{subbase}$ in Figure 43, Figure 44, and Figure 45 respectively. Semivariograms based on the long sparse data from MI I94 TS1a are shown in Figure 46 to Figure 48. Similar comparison of sparse and dense datasets is provided for MI I-96 TS1 (dense) and MI I-96 TS2 (sparse) datasets in Figure 49 to Figure 56.

The summarized spatial variability characteristics show range values between 2 m and 11 m for dense gridded datasets taken over a relatively small area versus range values between 15 m to 45 m for sparse datasets taken over relatively large areas.The longer ranges in the sparse dataset compared to shorter ranges calculated using the dense grid dataset suggests that there is a nested structure in the data with both short and long range spatial continuity on the measured properties.

**Table 14. Directional spatial variability characteristics summary on four test sections**

| Properties | Sampling type | Small Dense | | Long Sparse | | Small Dense | | Long Sparse | |
|---|---|---|---|---|---|---|---|---|---|
| Properties | Direction | MI I-94 TS1b | | MI I-94 TS1a | | MI I-96 TS1 | | MI I-96 TB2 | |
| | | Sill $(C+C_0)$ | Range (a or a'), m | Sill $(C+C_0)$ | Range (a or a'), m | Sill $(C+C_0)$ | Range (a or a'), m | Sill $(C+C_0)$ | Range (a or a'), m |
| $E_{LWD-Z3}$ (MPa) | Transverse | 59.1 | 11.0 | | | 165.3 | 2.6 | | |
| | Longitudinal | 63.0 | 3.0 | 206.4 | 38.3 | 203.5 | 8.3 | | |
| $E_{FWD-K3}$ (MPa) | Transverse | | | | | | | | |
| | Longitudinal | | | | | | | 6046.3 | 22.5 |
| $\gamma_d$ (kN/m$^3$) | Transverse | 0.35 | 2.3 | | | 0.67 | 7.5 | | |
| | Longitudinal | 0.62 | 9.9 | 0.35 | 33.2 | 0.17 | 2.2 | 0.63 | 15.4 |
| $w$ (%) | Transverse | | | | | 1.406 | 3.5 | | |
| | Longitudinal | | | 0.157 | 27.0 | 0.832 | 5.4 | 0.960 | 23.2 |
| DCPI$_{subbase}$ (mm/blow) | Transverse | 1.20 | 1.7 | | | 30.2 | 4.3 | | |
| | Longitudinal | 1.30 | 2.2 | 288.2 | 45.4 | 28.0 | 4.6 | | |
| DCPI$_{subgrade}$ (mm/blow) | Transverse | | | | | 5.9 | 1.1 | | |
| | Longitudinal | | | 2.1 | 31.7 | 4.2 | 2.3 | | |
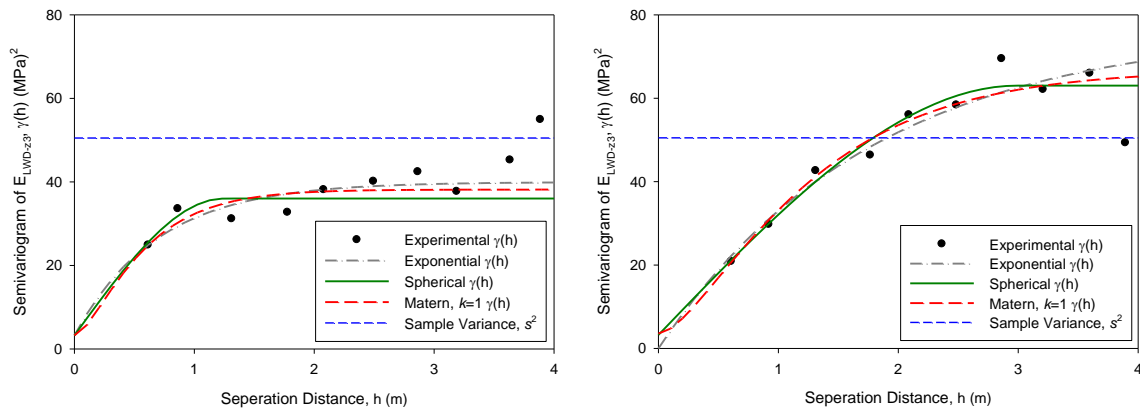


**Figure 43. Experimental γ(h) of E$_{LWD-Z3}$ on MI I-94 TS1b in transverse direction (left) and longitudinal direction (right)**
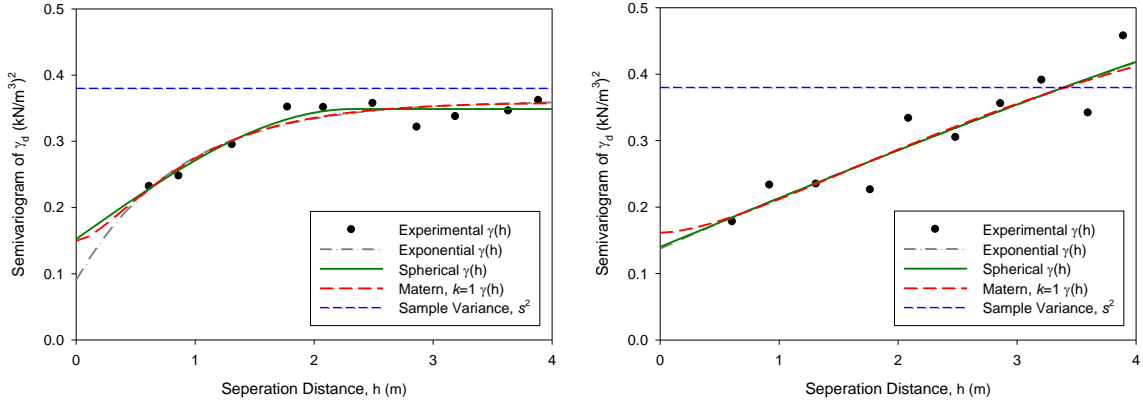
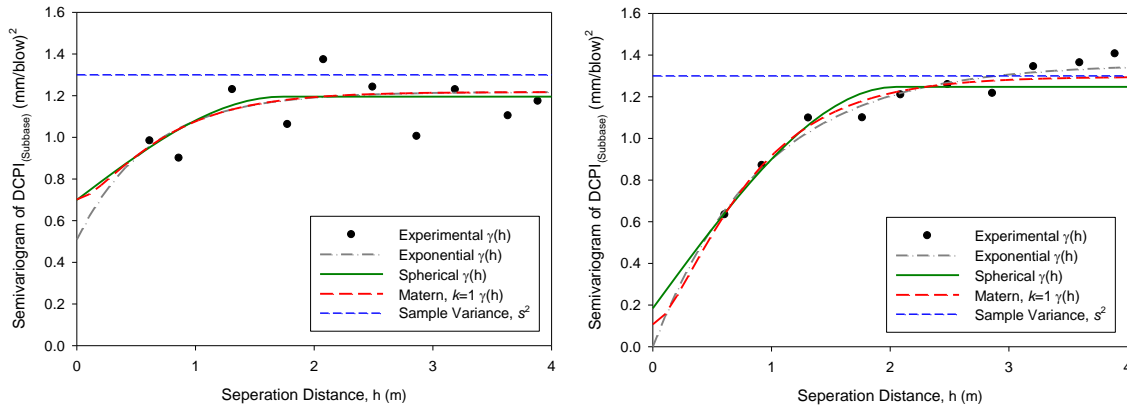**Figure 44. Experimental γ(h) of γd on MI I-94 TS1b in transverse direction (left) and longitudinal direction (right)**



**Figure 45. Experimental γ(h) of DCPIsubbase on MI I-94 TS1b in transverse direction (left) and longitudinal direction (right)**



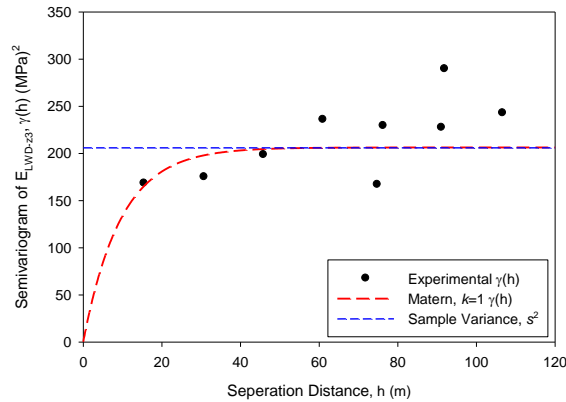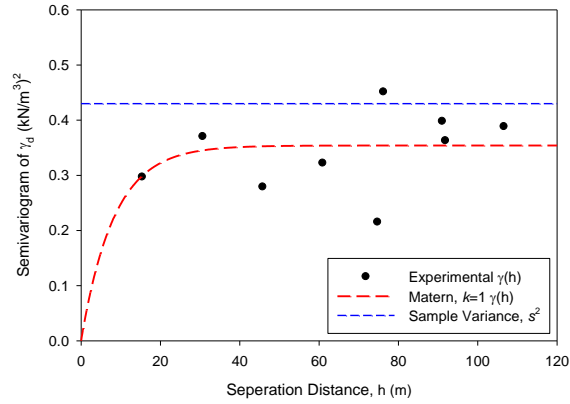**Figure 46. Experimental γ(h) of ELWD-Z3 on MI I-94 TS1a in longitudinal direction**

48

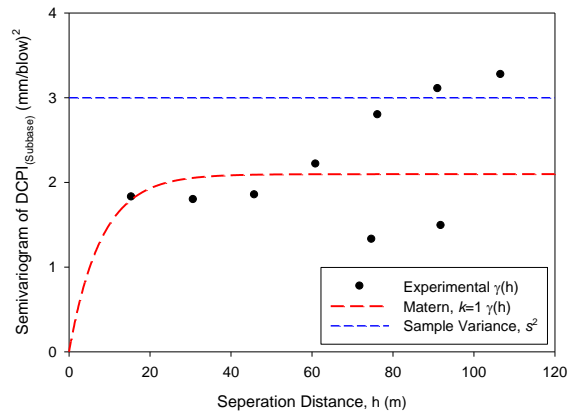**Figure 47. Experimental γ(h) of γ$_d$ on MI I-94 TS1a in longitudinal direction**



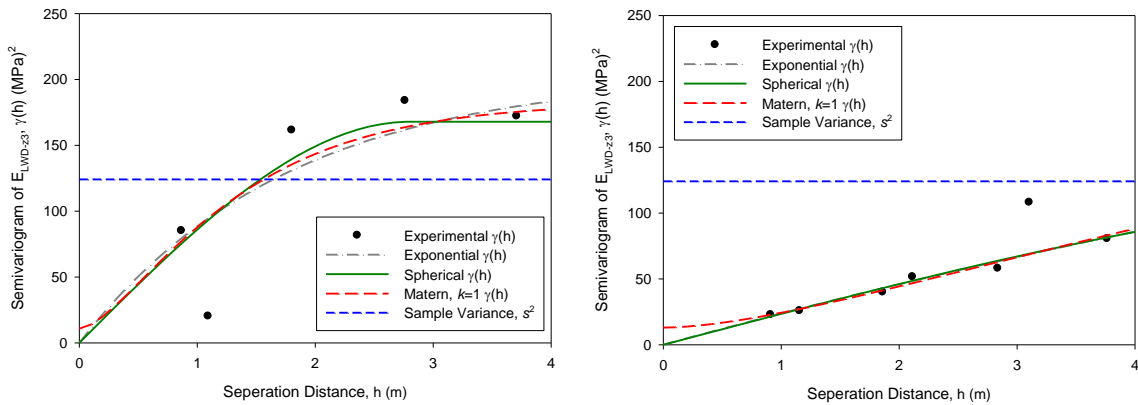**Figure 48. Experimental γ(h) of DCPI$_{subbase}$ on MI I-94 TS1a in longitudinal direction**



**Figure 49. Experimental γ(h) of E$_{LWD-z3}$ on MI I-96 TS1 in transverse direction (left) and longitudinal direction (right)**
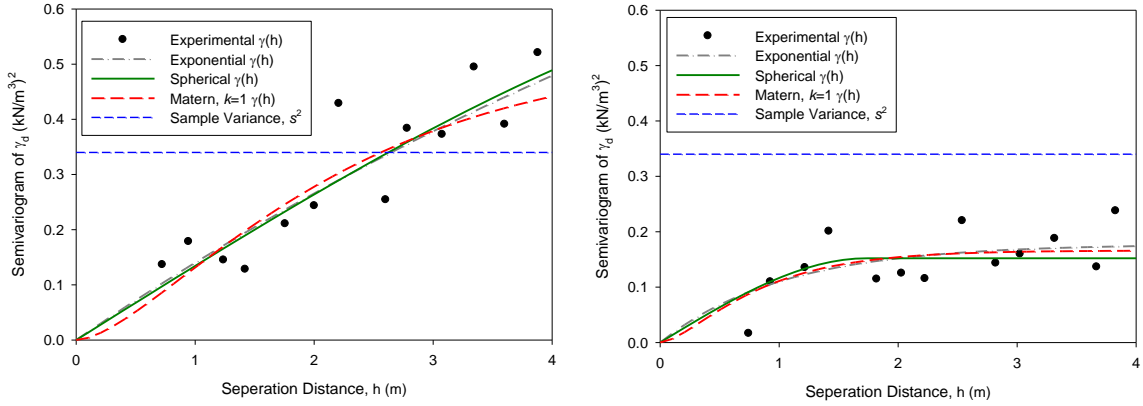
49

**Figure 50. Experimental γ(h) of γ_d on MI I-96 TS1 in transverse direction (left) and longitudinal direction (right)**



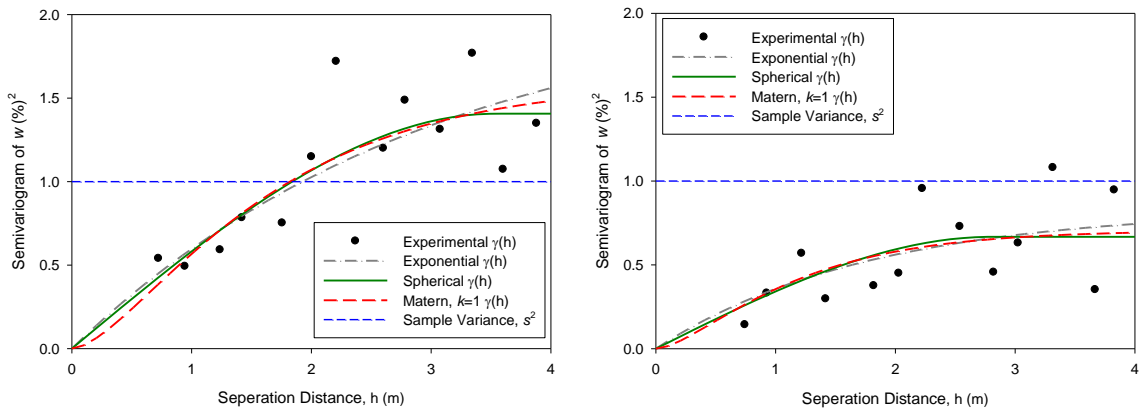**Figure 51. Experimental γ(h) of *w* on MI I-96 TS1 in transverse direction (left) and longitudinal direction (right)**



**Figure 52. Experimental γ(h) of DCPI_subbase on MI I-96 TS1 in transverse direction (left) and longitudinal direction (right)**

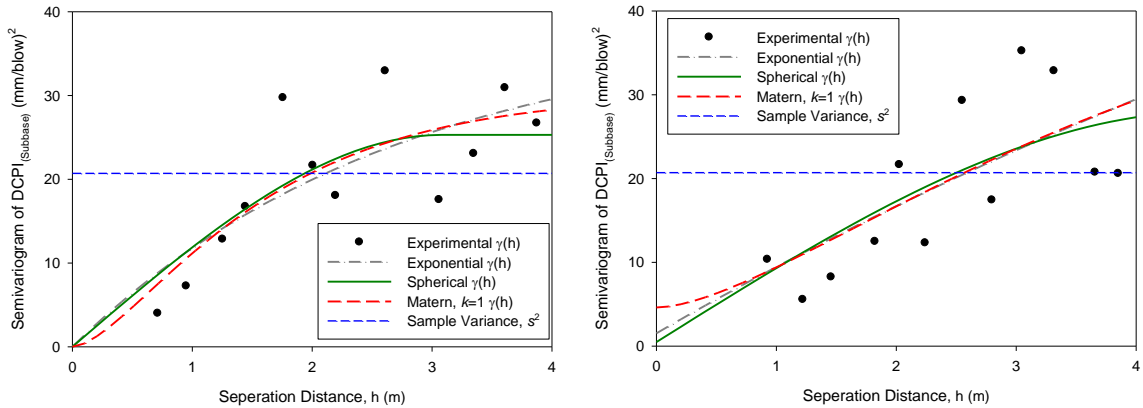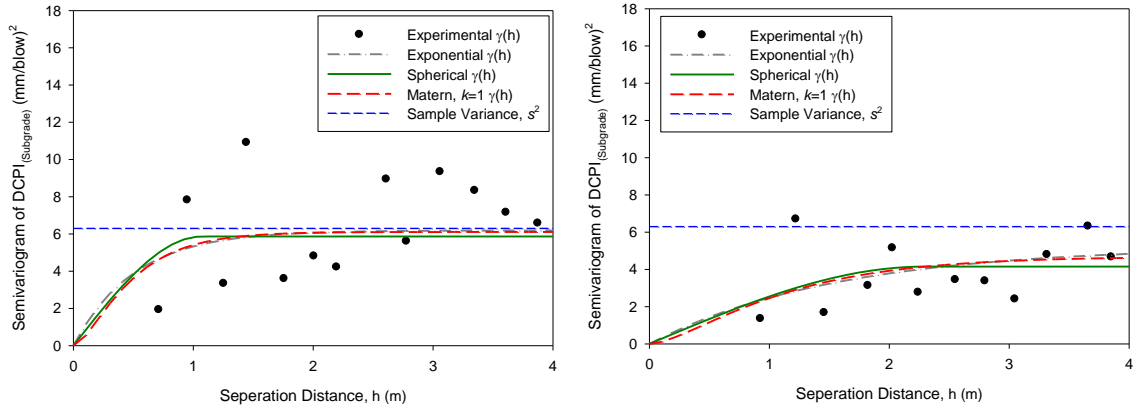**Figure 53. Experimental γ(h) of DCPI<sub>subgrade</sub> on MI I-96 TS1 in transverse direction (left) and longitudinal direction (right)**
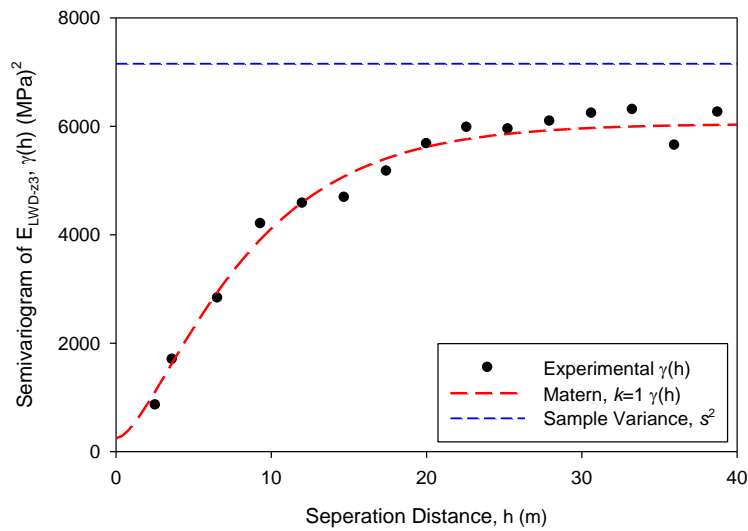


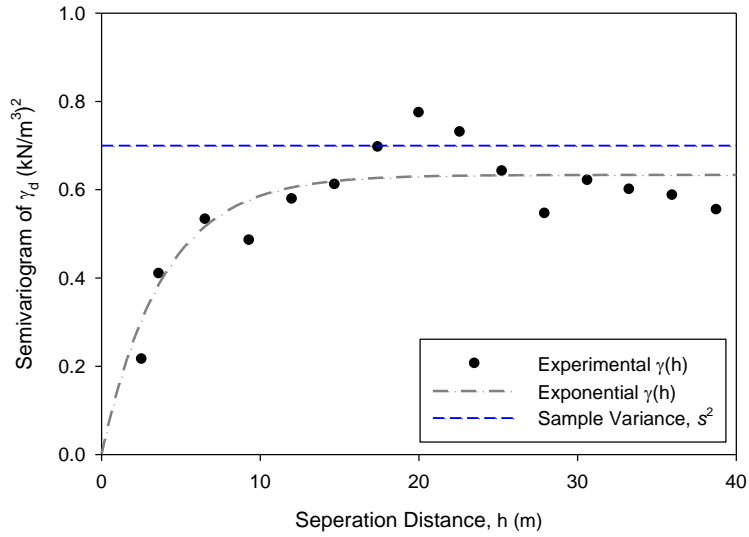**Figure 54. Experimental γ(h) of E<sub>LWD-Z3</sub> on MI I-96 TS2 in longitudinal direction**

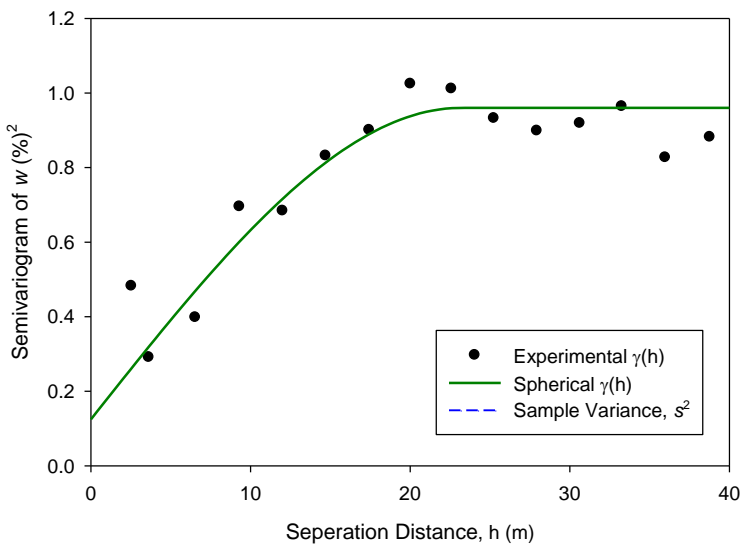**Figure 55. Experimental γ(h) of γ$_d$ on MI I-96 TS2 in longitudinal direction**



**Figure 56. Experimental γ(h) of *w* on MI I-96 TS2 in longitudinal direction**

# CHAPTER 5. SUMMARY AND CONCLUSIONS

In this report, results from selected field studies were analyzed for a more in-depth analysis of spatial variability and assess anisotropy in the different measurements. The following measurement parameters were assessed: a) elastic modulus determined from the light weight deflectometer (LWD) test ($E_{LWD-Z3}$), b) dynamic cone penetration index (DCPI) of subbase layer and subgrade layers ($DCPI_{subbase}$, and $DCPI_{subgrade}$) using dynamic cone penetrometer (DCP) test, and c) dry unit weight ($\gamma_d$) and moisture content ($w$) determined from the nuclear gauge (NG) test method. Results were analyzed on test sections where two different sampling methods were followed: a) dense grid sampling with spacing less than 1 m over a relatively short area (< 10 m x 10 m area) and b) sparse sampling with test locations separated by 4 to 5 m and over a relative large area (100 to 500 m).

Detailed geostatistical analysis procedures are presented in this report to provide a guide to study spatial variability of pavement foundation properties with consideration of choosing the best fitted semivariogram model and characterization of anisotropic behavior. Anisotropy in pavement foundation properties is assessed using directional semivarigrams in comparison with omnidirectional experimental semivariograms, rose diagrams (identifying semivarigoram range values in different directions), semivariogram maps, and semivariogram contour maps.

Spatial variability analysis on dense gridded test sections showed that different anisotropic major directions could be expected in different test areas. The dense gridded MI I-94 TS1b showed that the transverse direction is more uniform than the longitudinal direction, but the dense gridded MI I-96 TS1 showed the opposite. Analysis on dense gridded sections showed that the correlation length is about 2 m to 3 m in the minor direction (less uniform) and the correlation length in the major direction is about 3 to 4 times as the minor direction. Different anisotropic behavior was identified in the dense gridded sections analyzed in this report. The identified behaviors represented a relatively small sampling area that equaled the width of the foundation layer and about the same length in the longitudinal direction. More data in the longitudinal direction in similar grid fashion is required to further analyze anisotropy.

Comparison of three theoretical semivariogram models (i.e., spherical, exponential, Whittle or Matern with k=1) revealed that there was no obvious best fitted model to describe the experimental semivariogram of dense gridded measurements. A nested model with an anisotropy ratio helps in estimating the values at unsampled locations with consideration of the correlation of data sampled at different locations. However, for the cases analyzed in this study, the isotropic or omnidirectional semivariogram model can work as well as an anisotropic semivariogram model in estimating the values at unsampled locations. Correctly calculating the experimental semivariogram (i.e., selection of appropriate separation distances and bin sizes) is more important than looking at minor differences between the different models.

Comparisons of directional semivariogram models from dense and sparse datasets from same project are also provided in this report. The summarized spatial variability characteristics showed range values between 2 m and 11 m for dense gridded datasets taken over a relatively small area versus range values between 15 m to 45 m for sparse datasets taken over relatively large areas.

Longer ranges represent more spatially continuous data with longer correlation lengths than shorter ranges. The longer ranges in the sparse dataset compared to shorter ranges calculated using the dense grid dataset suggests that there is a nested structure in the data with both short and long range spatial continuity of the measured properties.

Collecting in situ point test measurements in dense grid pattern (with < 1 m separation distance between test points) over long distances is a significant effort. Properly calibrated roller-integrated intelligent compaction measurements that provide virtually 100% coverage of the pavement foundation layer properties can be an excellent data source to properly analyze and assess spatial variability and anisotropy aspects in the future.

# REFERENCES

ACPA. (2008). "Uniform support in concrete pavement structures," *Concrete Pavement Technology Series, TS201.1P*, American Concrete Pavement Association (ACPA), Skokie, IL.

Bivand, R. S., Pebesma, E., and Gómez-Rubio, V. (2013). Applied Spatial Data Analysis with R, Springer, New York.

Brand, A.S., Roesler, J.R., Chavan, H., and Evangelista, F. (2014). "Improving the Foundation Layers for Pavements: Effects of a Non-Uniform Subgrade Support on the Responses of Concrete Pavement.", InTrans Project 09-352, FHWA Pooled Fund Study TPF-5(183), Iowa State University, Ames, IA.

Clark, I., and Harper, W. V. (2002). Practical Geostatistics 2000, Ecosse North America Llc, Columbus, Ohio

Cressie, N. (1985). "Fitting variogram models by weighted least squares." Journal of the International Association for Mathematical Geology, 17(5), 563-586.

Cressie, N. A. C. (1993). Statistics for spatial data / Noel A.C. Cressie, New York : J. Wiley, New York

Eriksson, M., and Siska, P. P. (2000). "Understanding Anisotropy Computations." Mathematical Geology, 32(6), 683-700.

Facas, N. W., Mooney, M. A., and Furrer, R. (2010). "Anisotropy in the Spatial Distribution of Roller-Measured Soil Stiffness." International Journal of Geomechanics, 10(4), 129-135.

Goovaerts, P. (1997). *Geostatistics for Natural Resources Evaluation*, Oxford University Press, Oxford, UK.

Griffiths, D. V., Fenton, G. A., and Manoharan, N. (2006). "Undrained bearing capacity of two-strip footings on spatially random soil." Intl. J. Geomech., 6 (6), 421–427.

Isaaks, E. H., and Srivastava, R. M. (1989). An introduction to applied geostatistics. Oxford University Press, New York.

Jian, X., Olea, R. A., and Yu, Y.-S. (1996). "Semivariogram modeling by weighted least squares." Computers & Geosciences, 22(4), 387-397.

Journel, A. G., and Huijbregts, C. J. (1978). Mining geostatistics, Academic Press.

Mostyn, G. R., and Li., K. S. (1993). "Probabilistic slope analysis: State-of-play." Probabilistic methods in geotechnical engineering, K. S. Li and S-C. R. Lo, eds., Balkema, Rotterdam, The Netherlands, 89–109.

Olea, R. (2006). "A six-step practical approach to semivariogram modeling." Stochastic Environmental Research and Risk Assessment, 20(5), 307-318.

Pebesma, E. J. (2001). "Gstat user's manual." gstat 2.5.1, Dept. of Physical Geography, Utrecht University, Utrecht, The Netherlands.

Phoon, K-K., Kulhawy, F. H., and Grigoriu, M. D. (2000). "Reliability based design for transmission line structure foundations." Comput. Geotech., 26(3–4), 169–346.

Vennapusa, P. (2004). "Determination of the Optimum Base Characteristics for Pavements," M.S. Thesis, Department of Civil Construction and Environmental Engineering, Iowa State University, Ames, Iowa.

Vennapusa, P., and D. J. White. (2009). "Comparison of light weight deflectometer measurements for pavement foundation materials." *Geotechnical Testing Journal*, ASTM, 32(3), 239-251.

White, D. J., Rupnow, T., and Ceylan, H. (2004). "Influence of subgrade/subbase nonuniformity on pavement performance." Proc., Geo-Trans 2004 – Geotechnical Engineering for Transportation Projects, Geotechnical Special Publication No. 126, ASCE, Los Angeles, Ca., 1058–1065.

Wackernagel, H. (2003). Multivariate geostatistics : an introduction with applications / Hans Wackernagel, Springer-Verlag Berlin Heidelberg, Berlin ; New York

Webster, R., and Oliver, M. A. (2007). Geostatistics for environmental scientists, Wiley, Chichester; Hoboken, NJ.

Zorn, G., 2003, *Operating manual: Light drop-weight tester ZFG2000*, Zorn Stendal, Germany.